

## A force-induced directional switch of a molecular motor enables parallel microtubule bundle formation

Maxim I. Molodtsov<sup>1,2,3,5</sup>, Christine Mieck<sup>1,5</sup>, Jeroen Dobbelaere<sup>2</sup>, Alexander Dammermann<sup>2</sup>, Stefan Westermann<sup>1,4,\*</sup> and Alipasha Vaziri<sup>1,2,3,6,7,\*</sup>

<sup>1</sup>Research Institute of Molecular Pathology, Dr. Bohr-Gasse 7, Vienna, 1030, Austria

<sup>2</sup>Max F. Perutz Laboratories, University of Vienna, Dr. Bohr-Gasse 9, Vienna, 1030, Austria

<sup>3</sup>Research Platform Quantum Phenomena & Nanoscale Biological Systems (QuNaBioS), Dr. Bohr-Gasse 7, Vienna, 1030, Austria

<sup>4</sup>Department of Molecular Genetics, University of Duisburg-Essen, Essen, 45117, Germany

<sup>5</sup> These authors contributed equally to this work.

<sup>6</sup> The Rockefeller University, 1230 York Avenue New York, NY 10065-6399, USA

<sup>7</sup> Lead contact

\* Correspondence should be addressed to S.W. ([stefan.westermann@uni-due.de](mailto:stefan.westermann@uni-due.de)) or A.V. ([vaziri@rockefeller.edu](mailto:vaziri@rockefeller.edu))

## SUMMARY

Microtubule organizing centers (MTOCs) nucleate microtubules that can grow autonomously in any direction. To generate bundles of parallel microtubules originating from a single MTOC, the growth of multiple microtubules needs to be coordinated, but the underlying mechanism is unknown. Here we show that a conserved two-component system consisting of the plus-end tracker EB1 and the minus-end directed molecular motor Kinesin-14 is sufficient to promote parallel microtubule growth. The underlying mechanism relies on the ability of Kinesin-14 to guide growing plus-ends along existing microtubules. The generality of this finding is supported by yeast, *Drosophila* and human EB1/Kinesin-14 pairs. We demonstrate that plus-end guiding involves a directional switch of the motor due to a force applied via a growing microtubule end. The described mechanism can account for the generation of parallel microtubule networks required for a broad range of cellular functions such as spindle assembly or cell polarization.

## INTRODUCTION

Reorganization of the microtubule cytoskeleton is important for cell division and cell growth. Microtubule associated proteins (MAPs) including molecular motors are required to organize microtubules (MT) into higher-order structures such as parallel and anti-parallel bundles (Heald et al., 1996; Surrey et al., 2001), which are essential for intracellular transport, regulation of cell polarity and growth (de Forges et al., 2012; Drummond and Cross, 2000) as well as cell division (McIntosh et al., 2012). Although different microtubule nucleation pathways exist (Dumont and Desai, 2012; Goshima et al., 2008; Petry and Vale, 2015), generally microtubule nucleation *in vivo* requires microtubule-organizing centers (MTOCs) such as centrosomes. Nucleation at an MTOC

leads initially to microtubules that are equally likely to grow in all directions (Huda et al., 2012; Luders and Stearns, 2007). However, how the set of subsequent molecular events that orchestrate the conversion of this initial isotropic growth leads to the formation of parallel microtubule bundles *in vivo* is a fundamental open question.

Microtubules can be rearranged by molecular motors (Daga et al., 2006; Goshima and Scholey, 2010; Janson et al., 2007). Kinesins can slide microtubules within bundles (Kapitein et al., 2005; Su et al., 2013), destabilize anti-parallel and stabilize parallel microtubule bundles (Braun et al., 2009; Fink et al., 2009). In budding yeast, growth of parallel bundles depends on kinesin-14 Kar3 (Gardner et al., 2008; Laporte et al., 2013; Maddox et al., 2003; Middleton and Carbon, 1994; Tanaka et al., 2005). However, little is known about the mechanisms by which motors could orient and build parallel bundles from microtubules nucleated in random directions from an MTOC.

Microtubules are guided along actin filaments to form bundles at the cell periphery (Huda et al., 2012; Molk and Bloom, 2006). A similar behavior can occur in artificial systems in which one microtubule is guided along another (Chen et al., 2014; Doodhi et al., 2014). However, whether such a mechanism can also occur *in vivo* and is indeed responsible for the microtubule reorganization required for cell division and cell growth, remains unclear.

Here we report on the discovery of a microtubule plus-end guiding activity of kinesin-14 motors, which is conserved across species, and can direct microtubule growth from a single MTOC resulting in parallel bundle growth. We show that kinesin-14 motors are recruited to the tips of growing microtubules via interaction with EB1 and guide polymerization of new microtubules along the existing bundles. During this process, the movement of the budding yeast kinesin-14 Cik1-Kar3 depends on a switch in the asymmetry of the potential landscape induced by binding of ATP. This

mechanism is different from the conventional kinesin-14 mechanism based on the rotation of the stalk and it allows small sub-piconewton forces to induce multiple back steps in the movement of the motor whereby its direction can be effectively reversed. Our data suggest that the *Drosophila* and human kinesin-14/EB1 pairs may employ a mechanism with similar features to achieve parallel microtubule growth. Our key result is that only two proteins with distinct biophysical properties are necessary and sufficient for the controlled and reversible formation of parallel microtubule bundles from a common MTOC.

## RESULTS

### **Parallel microtubule bundles in yeast are maintained dynamically and depend on the presence of Kar3**

We used the mating projection (shmoo) of budding yeast as a model system to identify components important for building a parallel microtubule bundle (Figure 1A). In alpha-factor arrested cells kinesin-14 Kar3-3xGFP, which exists mostly as heterodimer with Cik1, localized to the cortical shmoo tip and the spindle pole body (SPB), as described previously (Maddox et al., 2003) and additionally could be found in the form of discrete foci along the shmoo tip bundle (Figure 1B), which consists of several microtubules (Maddox et al., 1999).

Surprisingly, we found that the Cik1-Kar3 moved along the microtubules in the bundle in the plus-end direction, opposite to the intrinsic minus-end directed motility of the motor (Figure 1C). As Cik1-Kar3 localization to the shmoo tip depends on the EB1 homolog Bim1 (Mieck et al., 2015) we reasoned that the plus-directed moving foci might represent the growing tips of microtubules decorated with Cik1-Kar3. Consistent with this idea, cells lacking Bim1 do not show Cik1-Kar3

localization along the bundle (Mieck et al., 2015), and, therefore the parallel microtubule bundle of the yeast shmoo tip is dynamically maintained in a process that involves plus-end directed transport of the Cik1-Kar3.

Imaging of yeast cells expressing GFP-Tubulin during alpha-factor arrest revealed that new microtubules nucleated from the SPB frequently appeared to grow along existing microtubules at the shmoo tip (Figure 1D). The fraction of these microtubules in wild type cells was ~ 33% (Figure 1E). This number was significantly reduced and indistinguishable from zero ( $p_{kar3\Delta} = 0.12$ ,  $p_{cik1\Delta} = 0.13$ ) in mutants that genetically lacked either Cik1 or Kar3. Thus, microtubule guiding was effectively eliminated, demonstrating that Cik1-Kar3 is responsible for promoting microtubule growth along existing microtubules. Since this activity is likely to depend on the plus-end tracker EB1, we set out to explore interaction between these molecules in more detail.

### **Cik1-Kar3 and the EB1 homologue Bim1 interact in a phospho-regulated manner**

To elucidate the topology of the motor-EB1 complex we generated a map of Lysine-Lysine distance restraints by performing chemical cross-linking followed by mass spectrometry of Cik1-Kar3 alone and in complex with the yeast EB1 analogue Bim1 (Figure 2A). As expected from the architecture of the Cik1-Kar3 heterodimer, the majority of cross-links between the proteins were found along the length of the stalk region. By contrast, only a few cross-links were assigned between the catalytically active motor domain of Kar3 and the motor homology domain of Cik1 (Figure 2A). In the three-protein complex with Bim1, the N-terminal domains of Cik1 (residues 1-360) and Kar3 (residues 1-386) were both found in proximity to Bim1's linker and EB homology domain (EBH), consistent with the observation that Bim1 fails to recruit Kar3 alone, monomeric Cik1 or

heterodimeric Vik1-Kar3, to MTs (Manning et al., 1999; Mieck et al., 2015; Page et al., 1994). Therefore, the N-terminal domains of Cik1 and Kar3 form a composite binding interface with EB1, spatially separated by the stalk from the catalytic and non-catalytic head domains (Figure 2A).

To investigate whether this interaction might be subject to regulation we mapped phosphorylation sites of native yeast Kar3 purified from different cell cycle stages. Intriguingly, all phosphorylation sites were located in the N-terminal domain of Kar3 (Figure 2B). In S-phase five of the identified phosphorylation sites matched the Cdc28/Cdk1 consensus sequence, consistent with Kar3 being a Cdk1 target (Ubersax et al., 2003). We confirmed that full length Kar3 but not a Kar3<sup>116-729</sup> mutant that lacked the N-terminal tail domain could be efficiently phosphorylated by Cdc28-Clb2 *in vitro* (Figure 2C). Given the confinement of Cdk1 sites to the N-terminal domain, we tested whether phosphorylation might regulate complex formation between Bim1 and Cik1-Kar3. When incubated together Cik1-Kar3 and Bim1 co-eluted during size exclusion chromatography (SEC) indicating a robust interaction (Figure 2D). Phosphorylation of Cik1-Kar3 by Cdc28 prior to SEC, however, was sufficient to disrupt complex formation as indicated by the altered elution profile.

### **Reconstitution of parallel microtubule growth *in vitro***

To recapitulate parallel microtubule bundle formation from an MTOC we adhered *Tetrahymena* pellicles as microtubule nucleation centers to the surface of a passivated cover glass and observed microtubule growth after addition of fluorescently labeled components by total internal reflection fluorescence microscopy (TIRF) (Figure 3A). In this system, pellicles nucleate many microtubules that have uniform polarity in all directions, mimicking microtubules grown from MTOCs *in vivo*

(Grishchuk et al., 2005; Lombillo et al., 1993). As all microtubule plus-ends grow outwards they define the directionality of motion for purified proteins on their lattices (Figure 3A).

In the absence of EB1, Cik1-Kar3 showed minus-end directed processive movement towards the pellicle where it accumulated (Figure 3B). Under conditions compatible with EB1-Motor interactions, recombinant budding yeast Bim1 displayed strong interaction not only with microtubule ends but also with the microtubule lattice, which obscured the interaction with the tip (Figure S1A). Therefore, we used the EB1 homologue from fission yeast, Mal3 (Figure 3C, Movie S1), which was able to recruit Cik1-Kar3 to the growing microtubule ends (Figure 3D). To confirm that the interaction between Mal3 and Cik1-Kar3 is similar to Bim1, we constructed a chimeric protein consisting of the microtubule-binding calponin-homology (CH) domains of Mal3 combined with the cargo-binding domain of Bim1, responsible for its interaction with Cik1-Kar3 tail (Figure S1B). This Mal3-Bim1 chimera showed a behavior indistinguishable from wild-type Mal3 *in vitro* (Figure S1C,D) and localized to microtubule-plus ends in both alpha-factor arrested and mitotic cells upon expression in yeast (Figure S1E,F).

### **Cik1-Kar3 guides the growth of new microtubule tips**

Strikingly the microtubule organization was drastically changed upon combination of Cik1-Kar3 and Mal3 in this assay. The growth of most new microtubules was guided along existing microtubules, resulting in parallel bundle growth similar to the *in vivo* observation (Movie S2). Bundle growth was evidenced by the directionality of Mal3 comets and the appearance of multiple plus ends in a single kymograph representation (Figure 3D,E).

In order to quantify this process we established an automated tracking and processing pipeline (Figure 3F). Tips of microtubules were tracked and naturally classified as either growing independently or guided along an existing bundle. In the presence of Cik1-Kar3 and Mal3 growth of more than 60% of microtubules was guided along others and frequently several microtubules formed a bundle (Figure 3G, Figure S2A). In the absence of Cik1-Kar3 this fraction was less than 20% (Figure 3G), and the formation of larger bundles was never observed (Figure S2B).

Automated processing revealed that the tips of guided microtubules had more Cik1-Kar3 associated with their tips compared to independent microtubules (Figure 3H). The increased amount of Cik1-Kar3 at the tips also correlated with a slower microtubule growth rate (Figure 3I). This led us to hypothesize that Cik1-Kar3 located at the growing tip of the guided microtubules crosslinks it to the lattice of a microtubule bundle and has the ability to slow down microtubule growth by generating a minus end directed force. To test this idea, we analyzed the rates of microtubule growth in the presence of ADP, a condition in which Cik1-Kar3 only weakly interacts with microtubules and cannot produce a counteracting force (Mieck et al., 2015) (Figure S2D). The amount of guided microtubules in this case was significantly smaller (Figure 3G), indicating that presence of ADP alone is insufficient for optimal parallel bundle formation. The fraction of microtubules that did undergo guided growth showed no detectable decrease of the growth rate as the amount of Cik1-Kar3 at their tips increased (Figure 3I) supporting our hypothesis that ability of the motor to actively move and resist its transport by the growing microtubule plus end is important for the efficient guided growth.

Next, we tested the effect of phosphorylation *in vitro*. We found Cdc28/Cdk1 phosphorylated Cik1-Kar3 no longer co-localized with Mal3 and moved in the minus end direction towards the pellicles,

while plus end tracking by Mal3 was unaffected (Figure 3J). Our analysis revealed no significant difference between the amount of microtubule bundle growth in the presence of phosphorylated Cik1-Kar3 and the absence of Cik1-Kar3 altogether (Figure 3G).

In order to understand how formation of parallel bundles could arise from the collective action of Mal3 and Cik1-Kar3 molecules, we performed numerical simulations (Movie S3, Methods) in which we assumed Cik1-Kar3 at a microtubule tip allows for capturing the adjacent microtubule and redirection of the growth. This allowed us to quantitatively reproduce the experimentally observed dynamics of microtubules in the presence of both molecules (Movie S4). Moreover, our simulations predicted that the efficiency of the bundling depends on the density of nucleation centers and microtubule dynamics, in quantitative agreement with the experimentally measured value (Figure 3G, dotted line, Figure S3).

Finally, to address whether Cik1-Kar3 can promote guided growth of microtubules in different orientations, we used a setup in which microtubules were nucleated from GMPCPP seeds immobilized on coverslips in all possible random directions (Figure S4A). We found that Cik1-Kar3 associated with Mal3 at the microtubule tip guides microtubule growth not only towards the plus end, but in this configuration also towards the minus end (Figure S4B-D), consistent with the ability of Cik1-Kar3 to align antiparallel microtubules along the spindle axis (Hepperla et al., 2014).

### **Cik1-Kar3 is a weak motor whose direction can be reversed by opposing force**

To investigate the biophysical basis for the ability of Cik1-Kar3 to switch its direction, we coupled 0.28  $\mu\text{m}$  size beads to Cik1-Kar3 motors and recorded their movement on taxol-stabilized microtubules using a fixed position optical trap (Figure 4A, Figure S5A-C). The fraction of binding

and moving beads as a function of the relative kinesin concentration followed a Poisson distribution, supporting the notion that a single Cik1-Kar3 heterodimer is sufficient to move the bead (Figure 4B). The average speed of Cik1-Kar3 was  $50 \pm 10$  nm/s in the direction of the minus-end. Increased loads slowed down the motor and induced more dissociation events. The highest force at which the average velocity across many molecules could be determined was not sufficient to stall the motor completely. The linear fit of the data indicated that the force at which average velocity drops to zero is  $\sim 0.25$  pN (Figure 4C).

Individual position traces showed discrete steps (Figure 4D), whose size was distributed around two major peaks at  $\sim \pm 8$  nm (Figure 4E). This indicated that Cik1-Kar3 makes discrete steps in the forward and the backward direction with a step size consistent with the periodicity of the microtubule lattice. The number of back steps was surprisingly high and multiple consecutive back steps were frequently observed. Thus, the overall directionality of the motor was due to more frequent minus-end directed steps (Figure 4D,E).

At 6 mM ATP, beads with single Cik1-Kar3 molecules detached easily, which made it challenging to study whether an opposing force can lead to the movement in reverse direction. At 6  $\mu$ M ATP the velocity of Cik1-Kar3 decreased to  $\sim 7$  nm/s (Figure 4F) and the dwell time increased  $\sim 4$  fold (Figure 4G-H), allowing us to visualize the transient movements of Cik1-Kar3 under external force. An opposing force led to more frequent backward steps of Cik1-Kar3 and thus to a net movement towards the plus-end (Figure 4I,J). The run length of the motors for the reverse direction was two times smaller than that of unloaded motors in the minus-end direction under the same conditions (Figure S5E,F). Thus, sub-piconewton opposing forces increase the frequency of plus-end directed steps and lead to a reversal of the motor's net direction of movement.

## Nucleotide dependent asymmetry of the Cik1-Kar3 – microtubule interaction potential facilitates

### Cik1-Kar3 movement

In order to dissect the mechanism of Cik1-Kar3 movement further, we investigated the detachment lifetime of the motor from the microtubule under external force in the absence of nucleotide and in the presence AMPPNP, a non-hydrolysable ATP analogue. We allowed beads coupled to single kinesin molecules to interact with microtubules for a brief moment, then applied a force in either the plus- or minus-end direction (Figure S5G) and measured the time to the detachment (Figure 5A, Figure S5H,I).

Surprisingly, in the absence of the nucleotide the lifetime of Cik1-Kar3 increased when the force was applied towards the plus-end (Figure 5B), and was reminiscent of ‘catch bonds’, whose interaction is enhanced by mechanical force (Thomas et al., 2008). The interaction could be overcome by forces above 0.5 pN, which led to a decrease in lifetimes irrespective of the force direction (Figure 5B). In the AMPPNP state direction was reversed: the lifetime increased for the minus-end directed forces (Figure 5C).

The observed detachment lifetimes can be accounted for by a model in which the energy barrier that a kinesin molecule needs to overcome to detach from the microtubule is non-symmetric (Thomas et al., 2008) (Figure 5D). The average bond lifetime is inversely proportional to the off-rate (Evans and Ritchie, 1997):

$$\tau(F) = \frac{1}{k_o(\exp(F(\frac{1}{2}D + \dots)/k_B T) + \exp(-F(\frac{1}{2}D - \dots)/k_B T))} \quad (1)$$

Here  $k_o$  is the off-rate in the absence of an external force,  $F$  – external force,  $D$  is the width of the kinesin-microtubule binding potential and  $\delta$  is the distance between the minimum and the midpoint of the potential well (Figure 5D).

Bayesian inference (Gelman et al., 2003) of the parameters from Equation 1 showed that when no nucleotide is bound to Cik1-Kar3, the minimum of the potential is shifted towards the plus end of the microtubule for  $\delta = 2.4 \pm 0.4$  nm. Binding of ATP reverses this asymmetry, and in this state, the minimum is shifted towards the minus end for  $\delta = -1.4 \pm 0.6$  nm (Figure S6A-B, Table S1).

We hypothesized that a change in the asymmetry of the interaction potential induced by ATP binding may underlie the mechanism by which Cik1-Kar3 moves towards the minus end. To test this idea we took advantage of the Cik1<sup>(1-360)</sup>-Kar3 mutant, which lacks non-catalytic head domain, can diffuse along microtubules, but is incapable of producing a directed movement (Mieck et al., 2015). The detachment lifetimes for the mutant showed no asymmetry under external force (Figures 5E,F), indicating that the interaction potentials were directionally symmetric in both, no NTP and the ATP bound states (Figure S6C-D, Table S1), supporting our idea.

### **Plus-end guiding activity is a conserved feature of Kinesin-14/EB1 pairs across species**

Interactions between Kinesin-14 and EB1 proteins are conserved across evolutionary distant organisms (Braun et al., 2013; Goshima et al., 2005). Therefore, we asked whether the respective pairs of human and *Drosophila* proteins are capable of promoting parallel microtubule growth by plus-end guiding.

In our *in vitro* assay (Figure 3A), *Drosophila* EB1 (dmEB1) showed similar to Mal3, plus-end tracking activity (Figure 6A). At similar conditions, *Drosophila* kinesin-14 Ncd crosslinked microtubules and alone promoted formation of bundles as evidenced by the accumulation of the motor along the length of microtubule bundles (Figure 6A). However, at higher salt concentration the majority of Ncd co-localized with dmEB1 at the microtubule ends, where it promoted plus-end guided microtubule growth as suggested by both appearance of multiple-end kymographs (Figure 6B) and quantification of guided growth using our automated pipeline (Figure 6C).

Human EB1 (hsEB1) autonomously tracked microtubule plus ends in our assay, although the weaker fluorescence indicated fewer EB1 molecules at the microtubule tips compared to Mal3 and dmEB1 (Figure 6D). When human kinesin-14 (HSET) was added to the system under conditions similar to Ncd it also supported formation of parallel bundles (Figure 6C).

Finally, in order to investigate whether *Drosophila* Ncd supports microtubule bundle growth by plus-end guiding *in vivo*, we established a *Drosophila* S2 cell line stably expressing low levels of EB1-GFP (Figure 6E). In mitotic cells, we tracked individual plus ends of microtubules and then used our pipeline to quantify the amount of plus-end guided microtubules for both astral and spindle microtubules. The amount of the plus-end guiding was more than two-fold higher for spindle compared to astral microtubules (Figure 6F,G). The Ncd RNAi knockdown led to a significant decrease of plus-end guiding for both types of microtubules (Figure 6G). This demonstrates that Ncd is necessary for efficient formation of parallel microtubule bundles during cell division, and taken together our results show that kinesin-14/EB1 system is necessary and sufficient for the formation of parallel microtubule arrays across species.

## DISCUSSION

### **Two conserved molecular components are sufficient for the growth of parallel microtubule bundles**

We have proposed and demonstrated both *in vivo* and *in vitro* a mechanism, which allows for the effective generation of parallel microtubule bundles from a single MTOC by the collective action of just two conserved molecular components. The mechanism redirects the growth of individual microtubules originating from an MTOC into bundles using the guiding activity of kinesin-14. Key molecular activities involved in this mechanism are summarized in Figure 7A-D.

*In vitro* reconstitution demonstrated that yeast Cik1-Kar3 leads to ~ 60% of guided microtubules in our assay. This value was consistent with our numerical simulations, which showed that the efficiency of bundling is limited by the density of the nucleation centers and the parameters of microtubule dynamics (Figure S3). The ability of *Drosophila* Ncd and human HSET to support plus-end guiding of microtubules was lower compared to Cik1-Kar3. We account this to the difference between the ability of Cik1-Kar3 to move processively as opposed to the non-processive movement of Ncd and HSET. Thus in comparison to Ncd and HSET, Cik1-Kar3 can accumulate at a higher density at an MTOC where capturing of new microtubule ends is facilitated with higher efficiency.

Previous experiments have demonstrated that kinesin-14s use an ATP-dependent rotation of the stalk to promote microtubule-microtubule sliding (Endres et al., 2006; Wendt et al., 2002). The ability of Ncd, HSET and Cik1-Kar3 to promote parallel microtubule growth as well as our single molecule analysis of Cik1-Kar3 suggest that during plus-end guiding kinesin-14 motors use a different motility mechanism, which relies on weak, diffusive interactions with the microtubule

lattice. Consistent with this idea, a single Ncd kinesin has been shown to undergo a diffusive movement along the microtubule lattice even in the presence of a trapping force (Furuta et al., 2013). Thus, during microtubule guiding, Ncd and HSET may use the diffusive motility, which is biased towards the plus end by the force exerted by a growing microtubule.

In our *in vitro* assay, the kinesin-14/EB1 system converted the growth of independent microtubules into bundles oriented in random directions (Figure 7E, Movie S2). In the yeast mating projection microtubules pointing to the shmoo can be selectively stabilized via cortical interactions. We asked whether such stabilization would promote the formation of a single parallel bundle, by simulating growing of microtubules from an SPB of a yeast cell and selectively reducing the catastrophe rate of microtubules directed towards the mating projection (Figure 7E, Methods). Our simulations showed that such a stabilization indeed promotes formation of a single shmoo tip bundle (Movie S5). By contrast, when no selective stabilization was assumed parallel bundles formed less efficiently and occurred more in random orientations (Movie S6, Figure 7F). This shows how the superposition of the EB1/kinesin-14 system with local microtubule dynamics control can lead to the efficient directional formation of parallel bundles.

### **Biophysical mechanism of budding yeast kinesin 14 Cik1-Kar3 movement**

Cik1-Kar3 is a heterodimer consisting of the kinesin-14 Kar3 with an active ATP motor domain and its partner protein Cik1, which possesses a motor-like fold but is catalytically inactive (Allingham et al., 2007; Manning et al., 1999; Page et al., 1994). We have previously shown that a single molecule of Cik1-Kar3 can support processive movement depending on the presence of the non-catalytic

head domain, but the molecular mechanism underlying such a processive movement remained unclear (Mieck et al., 2015).

Our current results favor a Brownian ratchet mechanism of the Cik1-Kar3 movement, in which the motor makes random steps in both plus- and minus-end directions. This is facilitated by the wide interaction potential (Table S1), which allows the molecule to remain weakly associated with the microtubule lattice and transition from one binding site to another as a whole without significant separation of the head domains, consistent with previous structural studies (Gonzalez et al., 2013).

Based on our observations we propose the following detailed model of Cik1-Kar3 movement. In the no NTP state Cik1-Kar3 experiences thermal forces from surrounding media that allow for the bound diffusion of Cik1-Kar3 on the microtubule spatially constrained to approximately the size of a single tubulin dimer (Figure S6A). The asymmetry of the potential results in longer and more frequent random excursions towards the minus comparing to the plus end (Figure S6A). Extensive minus-end directed movements are rectified by the corresponding change of the potential landscape induced by ATP binding leading to a productive eight-nm step (Figure S6B). After an ATP is hydrolyzed, Cik1-Kar3 enters a weakly bound diffusive state, which can produce random steps in both directions (Mieck et al., 2015) (Figure S6C). A plus-end directed external force hinders the diffusion of the motor in non-NTP state leading to fewer productive minus-end directed steps and biases the movement towards the plus end in the ADP state (Figure S6A-C).

This mechanism implies that not every ATP hydrolysis event leads to a productive step, and several ATP molecules are required on average to produce one eight-nm step. This is consistent with our bulk ATPase measurements, which show a fast steady-state kinetics ( $k_{cat}=14\text{ s}^{-1}$ ) suggesting that on average more than two ATP molecules are used per each 8 nm movement (Figure S7). This also

shows that movement of Cik1-Kar3 relies less on ATP coupling and represents a quantitatively different mechanism from the tight coupling mechanism employed by other kinesins (Okada et al., 2003; Schnitzer and Block, 1997).

### **Forces applied by growing microtubule tips promote formation of microtubule bundles**

Our data indicate that a growing microtubule tip applies a force to kinesin-14, reversing its direction of movement from the minus-end towards the plus-end. This is supported by our single molecule experiments, which showed that Cik1-Kar3 generates forces much smaller than those by conventional kinesins (Carter and Cross, 2005; Svoboda and Block, 1994) and that Cik1-Kar3 is a weak motor whose directionality can be modulated by an external force (Figure 4).

A previous study aimed to measure the force generated by single kinesin-14 Ncd failed to observe a clear evidence for force production but suggested any involved force to be below 1 pN (Furuta et al., 2013). This is consistent with our findings showing that Cik1-Kar3 easily detaches at forces above 0.5 pN, while similar or smaller forces can induce multiple back steps causing effectively a reversal of the direction of Cik1-Kar3. Therefore, a single polymerizing microtubule tip, which can resist up to 5 pN force (Dogterom and Yurke, 1997) is sufficient to overpower several kinesin-14 molecules working in parallel.

The force generated by the microtubule polymerization must be transduced to Cik-Kar3 by the EB1 molecules associated with the growing microtubule tip. This is likely related to the ability of EB1 to preferentially bind near the plus-end tips of growing microtubules and diffuse along the microtubule lattice (Bieling et al., 2007; Forth et al., 2014). Our data demonstrate that EB1 interaction with the microtubule allows the microtubule polymerization to apply a mechanical

force onto the kinesin-14 located at its tip and switch the direction of kinesin movement resulting in the growth of parallel microtubule bundles.

## **Conclusions**

Steering of microtubule growth is important for the organization of microtubule arrays. Our study demonstrates that kinesin-14s possess distinct biophysical properties, which in combination with their binding partner EB1 allow guided growth of MTs from a common MTOC. The mechanism of yeast Cik1-Kar3 movement described here does not rely on the kinesin-14 typical neck rotation towards the minus end upon ATP binding (Cope et al., 2013; Endres et al., 2006; Wendt et al., 2002) demonstrating that Kar3 can support very different types of motility mechanisms. This must also be true for kinesin-14 from other organisms, Ncd and HSET, which we show can support a similar type of motility. Our discovered mechanism might have very general implications and be used not only within the kinesin superfamily but also across other families of motors such as myosins and dyneins (Sckolnick et al., 2013; Tripathy et al., 2014). This phenomenon extends the hitherto known mechanistic repertoire of how chemical energy is used to produce directed movement at the nanoscale in a biological environment. Further it provides an example, which might inspire future work on the design of artificial molecular motors (Goel and Vogel, 2008; Goodman et al., 2012).

The reported mechanism of parallel bundle formation could be of general relevance for a broad range of cellular functions relying on directional microtubule growth such as mitotic spindle formation and kinetochore-microtubule interactions. Furthermore, reversal of direction and compliance under opposing force may be a general feature that allows functionalities distinct from other kinesin molecules that move with the well-established hand-over-hand mechanism. This

property might be important not only in building microtubule arrays but also, for example, during directional instability of chromosome movements where direction of the chromosome motion needs to change without losing the connection to the kinetochore microtubule. In the future, the extension of our reconstitution approach by including additional proteins promises to yield further mechanistic understanding of the basic organization principles of higher-order microtubule structures in metazoans.

## **METHODS AND RESOURCES**

Detailed methods are provided in the online version of this paper and include the following:

### **KEY RESOURCES TABLE**

- CONTACT FOR REAGENT AND RESOURCE SHARING
- EXPERIMENTAL MODEL AND SUBJECT DETAILS
- METHOD DETAILS
- QUANTIFICATION AND STATISTICAL ANALYSIS
- DATA AND SOFTWARE AVAILABILITY
- ADDITIONAL RESOURCES

### **SUPPLEMENTAL INFORMATION**

Supplemental Information includes seven Supplemental Figures, six Movies and one Supplemental Table.

## **AUTHOR CONTRIBUTIONS**

M.I.M and C.M. performed experiments, M.I.M. and A.V. designed and built optical setups, M.I.M. wrote control software, data acquisition and data analysis software, M.I.M. and C.M. analyzed data, M.I.M. developed mathematical modeling, M.I.M, S.W. and A.V. wrote the manuscript, M.I.M, S.W. and A.V. designed and conceived experiments.

## **ACKNOWLEDGMENTS**

We thank M. Colombini and the IMP mechanical workshop for manufacturing of equipment used in this study. We thank G. Litos, K. Mochizuki, K. Kataoka, J. I. Artola and L.T. Muurmans for help with experiments, A. Shnol and F. Ataulkhanov for providing QPD electronics, E. Rampler and K. Mechtler for performing mass spectrometry experiments. We thank T. Surrey, G. Goshima, T. Kapoor and C. Walczak for kindly providing the expression plasmids for Mal3, dmEB1, Ncd, hsEB1 and HSET, respectively. M. I. M. and J. D. acknowledge the VIPS Program of the Austrian Federal Ministry of Science and Research and the City of Vienna. This work received funding from the European Research Council under the European Community's Seventh Framework Programme (SW FP7/2007-2013)/ERC grant agreement number [203499], from the Austrian Science Fund FWF (SW, SFB F34-B03) and the Austrian Research Promotion Agency (FFG), from the Vienna Science and Technology Fund (WWTF) project VRG10-11 and LS14-009, the Human Frontiers Science Program

Project RGP0041/2012, the Research Platform Quantum Phenomena and Nanoscale Biological Systems (QuNaBioS) and Research Institute of Molecular Pathology (IMP). The IMP is funded by Boehringer Ingelheim.

## REFERENCES

- Allingham, J.S., Sproul, L.R., Rayment, I., and Gilbert, S.P. (2007). *Vik1 modulates microtubule-Kar3 interactions through a motor domain that lacks an active site.* *Cell* **128**, 1161-1172.
- Bieling, P., Laan, L., Schek, H., Munteanu, E.L., Sandblad, L., Dogterom, M., Brunner, D., and Surrey, T. (2007). *Reconstitution of a microtubule plus-end tracking system in vitro.* *Nature* **450**, 1100-1105.
- Braun, M., Drummond, D.R., Cross, R.A., and McAinsh, A.D. (2009). *The kinesin-14 Klp2 organizes microtubules into parallel bundles by an ATP-dependent sorting mechanism.* *Nat Cell Biol* **11**, 724-730.
- Braun, M., Lansky, Z., Bajer, S., Fink, G., Kasprzak, A.A., and Diez, S. (2013). *The human kinesin-14 HSET tracks the tips of growing microtubules in vitro.* *Cytoskeleton (Hoboken)* **70**, 515-521.
- Carter, N.J., and Cross, R.A. (2005). *Mechanics of the kinesin step.* *Nature* **435**, 308-312.
- Chen, Y., Rolls, M.M., and Hancock, W.O. (2014). *An EB1-kinesin complex is sufficient to steer microtubule growth in vitro.* *Curr Biol* **24**, 316-321.
- Cope, J., Rank, K.C., Gilbert, S.P., Rayment, I., and Hoenger, A. (2013). *Kar3Vik1 uses a minus-end directed powerstroke for movement along microtubules.* *PLoS One* **8**, e53792.
- Daga, R.R., Lee, K.G., Bratman, S., Salas-Pino, S., and Chang, F. (2006). *Self-organization of microtubule bundles in anucleate fission yeast cells.* *Nat Cell Biol* **8**, 1108-1113.

de Forges, H., Bouissou, A., and Perez, F. (2012). Interplay between microtubule dynamics and intracellular organization. *Int J Biochem Cell Biol* 44, 266-274.

Dogterom, M., and Yurke, B. (1997). Measurement of the force-velocity relation for growing microtubules. *Science* 278, 856-860.

Doodhi, H., Katrukha, E.A., Kapitein, L.C., and Akhmanova, A. (2014). Mechanical and geometrical constraints control kinesin-based microtubule guidance. *Curr Biol* 24, 322-328.

Drummond, D.R., and Cross, R.A. (2000). Dynamics of interphase microtubules in *Schizosaccharomyces pombe*. *Curr Biol* 10, 766-775.

Dumont, J., and Desai, A. (2012). Acentrosomal spindle assembly and chromosome segregation during oocyte meiosis. *Trends Cell Biol* 22, 241-249.

Endres, N.F., Yoshioka, C., Milligan, R.A., and Vale, R.D. (2006). A lever-arm rotation drives motility of the minus-end-directed kinesin Ncd. *Nature* 439, 875-878.

Evans, E., and Ritchie, K. (1997). Dynamic strength of molecular adhesion bonds. *Biophys J* 72, 1541-1555.

Fink, G., Hajdo, L., Skowronek, K.J., Reuther, C., Kasprzak, A.A., and Diez, S. (2009). The mitotic kinesin-14 Ncd drives directional microtubule-microtubule sliding. *Nat Cell Biol* 11, 717-723.

Forth, S., Hsia, K.C., Shimamoto, Y., and Kapoor, T.M. (2014). Asymmetric friction of nonmotor MAPs can lead to their directional motion in active microtubule networks. *Cell* 157, 420-432.

Furuta, K., Furuta, A., Toyoshima, Y.Y., Amino, M., Oiwa, K., and Kojima, H. (2013). Measuring collective transport by defined numbers of processive and nonprocessive kinesin motors. *Proc Natl Acad Sci U S A* 110, 501-506.

Gardner, M.K., Haase, J., Myhre, K., Molk, J.N., Anderson, M., Joglekar, A.P., O'Toole, E.T., Winey, M., Salmon, E.D., Odde, D.J., *et al.* (2008). The microtubule-based motor Kar3 and plus end-binding protein Bim1 provide structural support for the anaphase spindle. *J Cell Biol* *180*, 91-100.

Gelman, A., Carlin, J.B., Stern, H.S., and Rubin, D.B. (2003). Bayesian data analysis (Chapman and Hall/CRC).

Goel, A., and Vogel, V. (2008). Harnessing biological motors to engineer systems for nanoscale transport and assembly. *Nat Nanotechnol* *3*, 465-475.

Gonzalez, M.A., Cope, J., Rank, K.C., Chen, C.J., Tittmann, P., Rayment, I., Gilbert, S.P., and Hoenger, A. (2013). Common mechanistic themes for the powerstroke of kinesin-14 motors. *J Struct Biol* *184*, 335-344.

Goodman, B.S., Derr, N.D., and Reck-Peterson, S.L. (2012). Engineered, harnessed, and hijacked: synthetic uses for cytoskeletal systems. *Trends Cell Biol* *22*, 644-652.

Goshima, G., Mayer, M., Zhang, N., Stuurman, N., and Vale, R.D. (2008). Augmin: a protein complex required for centrosome-independent microtubule generation within the spindle. *J Cell Biol* *181*, 421-429.

Goshima, G., Nedelec, F., and Vale, R.D. (2005). Mechanisms for focusing mitotic spindle poles by minus end-directed motor proteins. *J Cell Biol* *171*, 229-240.

Goshima, G., and Scholey, J.M. (2010). Control of mitotic spindle length. *Annu Rev Cell Dev Biol* *26*, 21-57.

Grishchuk, E.L., Molodtsov, M.I., Ataulakhanov, F.I., and McIntosh, J.R. (2005). Force production by disassembling microtubules. *Nature* *438*, 384-388.

Heald, R., Tournebize, R., Blank, T., Sandaltzopoulos, R., Becker, P., Hyman, A., and Karsenti, E. (1996). Self-organization of microtubules into bipolar spindles around artificial chromosomes in *Xenopus* egg extracts. *Nature* 382, 420-425.

Hepperla, A.J., Willey, P.T., Coombes, C.E., Schuster, B.M., Gerami-Nejad, M., McClellan, M., Mukherjee, S., Fox, J., Winey, M., Odde, D.J., *et al.* (2014). Minus-end-directed Kinesin-14 motors align antiparallel microtubules to control metaphase spindle length. *Dev Cell* 31, 61-72.

Huda, S., Soh, S., Pilans, D., Byrska-Bishop, M., Kim, J., Wilk, G., Borisy, G.G., Kandere-Grzybowska, K., and Grzybowski, B.A. (2012). Microtubule guidance tested through controlled cell geometry. *J Cell Sci* 125, 5790-5799.

Janson, M.E., Loughlin, R., Loiodice, I., Fu, C., Brunner, D., Nedelec, F.J., and Tran, P.T. (2007). Crosslinkers and motors organize dynamic microtubules to form stable bipolar arrays in fission yeast. *Cell* 128, 357-368.

Jaqaman, K., Loerke, D., Mettlen, M., Kuwata, H., Grinstein, S., Schmid, S.L., and Danuser, G. (2008). Robust single-particle tracking in live-cell time-lapse sequences. *Nat Methods* 5, 695-702.

Kapitein, L.C., Peterman, E.J., Kwok, B.H., Kim, J.H., Kapoor, T.M., and Schmidt, C.F. (2005). The bipolar mitotic kinesin Eg5 moves on both microtubules that it crosslinks. *Nature* 435, 114-118.

Kerssemakers, J.W.J., Munteanu, E.L., Laan, L., Noetzel, T.L., Janson, M.E., and Dogterom, M. (2006). Assembly dynamics of microtubules at molecular resolution. *Nature* 442, 709-712.

Laporte, D., Courtout, F., Salin, B., Ceschin, J., and Sagot, I. (2013). An array of nuclear microtubules reorganizes the budding yeast nucleus during quiescence. *J Cell Biol* 203, 585-594.

Lombillo, V.A., Coue, M., and McIntosh, J.R. (1993). In vitro motility assays using microtubules tethered to *Tetrahymena* pellicles. *Methods Cell Biol* 39, 149-165.

Luders, J., and Stearns, T. (2007). Microtubule-organizing centres: a re-evaluation. *Nat Rev Mol Cell Biol* 8, 161-167.

Maddox, P., Chin, E., Mallavarapu, A., Yeh, E., Salmon, E.D., and Bloom, K. (1999). Microtubule dynamics from mating through the first zygotic division in the budding yeast *Saccharomyces cerevisiae*. *J Cell Biol* 144, 977-987.

Maddox, P.S., Stemple, J.K., Satterwhite, L., Salmon, E.D., and Bloom, K. (2003). The minus end-directed motor Kar3 is required for coupling dynamic microtubule plus ends to the cortical shmoo tip in budding yeast. *Curr Biol* 13, 1423-1428.

Manning, B.D., Barrett, J.G., Wallace, J.A., Granok, H., and Snyder, M. (1999). Differential regulation of the Kar3p kinesin-related protein by two associated proteins, Cik1p and Vik1p. *J Cell Biol* 144, 1219-1233.

McIntosh, J.R., Molodtsov, M.I., and Ataullakhanov, F.I. (2012). Biophysics of mitosis. *Q Rev Biophys* 45, 147-207.

Middleton, K., and Carbon, J. (1994). KAR3-encoded kinesin is a minus-end-directed motor that functions with centromere binding proteins (CBF3) on an in vitro yeast kinetochore. *Proc Natl Acad Sci U S A* 91, 7212-7216.

Mieck, C., Molodtsov, M.I., Drzewicka, K., van der Vaart, B., Litos, G., Schmauss, G., Vaziri, A., and Westermann, S. (2015). Non-catalytic motor domains enable processive movement and functional diversification of the kinesin-14 Kar3. *Elife* 4, e04489.

Molk, J.N., and Bloom, K. (2006). Microtubule dynamics in the budding yeast mating pathway. *J Cell Sci* 119, 3485-3490.

Okada, Y., Higuchi, H., and Hirokawa, N. (2003). Processivity of the single-headed kinesin KIF1A through biased binding to tubulin. *Nature* 424, 574-577.

Page, B.D., Satterwhite, L.L., Rose, M.D., and Snyder, M. (1994). Localization of the Kar3 kinesin heavy chain-related protein requires the Cik1 interacting protein. *J Cell Biol* 124, 507-519.

Petry, S., and Vale, R.D. (2015). Microtubule nucleation at the centrosome and beyond. *Nat Cell Biol* 17, 1089-1093.

Schnitzer, M.J., and Block, S.M. (1997). Kinesin hydrolyses one ATP per 8-nm step. *Nature* 388, 386-390.

Skolnick, M., Kremmentsova, E.B., Warshaw, D.M., and Trybus, K.M. (2013). More than just a cargo adapter, melanophilin prolongs and slows processive runs of myosin Va. *J Biol Chem* 288, 29313-29322.

Su, X., Arellano-Santoyo, H., Portran, D., Gaillard, J., Vantard, M., Thery, M., and Pellman, D. (2013). Microtubule-sliding activity of a kinesin-8 promotes spindle assembly and spindle-length control. *Nat Cell Biol* 15, 948-957.

Surrey, T., Nedelec, F., Leibler, S., and Karsenti, E. (2001). Physical properties determining self-organization of motors and microtubules. *Science* 292, 1167-1171.

Svoboda, K., and Block, S.M. (1994). Force and velocity measured for single kinesin molecules. *Cell* 77, 773-784.

Tanaka, K., Mukae, N., Dewar, H., van Breugel, M., James, E.K., Prescott, A.R., Antony, C., and Tanaka, T.U. (2005). Molecular mechanisms of kinetochore capture by spindle microtubules. *Nature* 434, 987-994.

Thomas, W.E., Vogel, V., and Sokurenko, E. (2008). Biophysics of catch bonds. *Annu Rev Biophys* 37, 399-416.

Tripathy, S.K., Weil, S.J., Chen, C., Anand, P., Vallee, R.B., and Gross, S.P. (2014). Autoregulatory mechanism for dynactin control of processive and diffusive dynein transport. *Nat Cell Biol* 16, 1192-1201.

Ubersax, J.A., Woodbury, E.L., Quang, P.N., Paraz, M., Blethrow, J.D., Shah, K., Shokat, K.M., and Morgan, D.O. (2003). Targets of the cyclin-dependent kinase Cdk1. *Nature* 425, 859-864.

Wendt, T.G., Volkmann, N., Skiniotis, G., Goldie, K.N., Muller, J., Mandelkow, E., and Hoenger, A. (2002). Microscopic evidence for a minus-end-directed power stroke in the kinesin motor *ncd*. *EMBO J* 21, 5969-5978.

## FIGURE LEGENDS

### **Figure 1. Cik1-Kar3 is required for building a parallel microtubule bundle at the yeast shmoo tip**

(A) Cartoon representing formation of a parallel microtubule bundle from microtubules nucleating in random directions at an MTOC. Bottom panel illustrates this process in a budding yeast cell during alpha factor arrest.

(B) Fluorescence images showing Cik1-Kar3 localizing along the shmoo tip bundle. SPB is labeled with Spc42-mCherry. Bright-field image shows the cell outline with characteristic shmoo. Diffuse Kar3-GFP fluorescence in the cell body is due to unbound motors.

(C) Kymographs corresponding to (B) show movement of Cik1-Kar3 in plus-end direction towards the shmoo. White arrows indicate individual events of moving Kar3-GFP.

(D) Time sequence of GFP-tubulin images at the shmoo tip in wild type cells. MT<sub>1</sub> shown with blue arrow forms a template. Growth of MT<sub>2</sub> microtubule indicated with red arrow is guided along MT<sub>1</sub>.

(E) Fraction of microtubules whose growth follows along existing shmoo tip bundle in wt (n = 50) and mutant cells lacking either Cik1 (n = 35) or Kar3 (n = 30). Error bars are SEM.

**Figure 2. The interaction between Bim1 and Cik1-Kar3 occurs via the tail and is negatively regulated by Cdk1**

(A) A proximity map showing intermolecular Lys-Lys crosslinks between Cik1-Kar3 and Bim1 identified by mass spectrometry. Numbers denote amino acid residues. Green color indicates motor and motor-homology domains of Kar3 and Cik1. Orange – CH domain of Bim1. Crosslinks between tails of Bim1 and Cik1-Kar3 are shown in light green.

(B) Identification of Kar3 phosphorylation sites by mass spectrometry in cells arrested in different cell cycle stages. Phosphorylation sites are indicated by residue numbers.

(C) Autoradiography and Coomassie gels show that Cik1-Kar3, but not the Cik1-Kar3<sup>116-729</sup> N-terminal deletion mutant is phosphorylated by Cdc28/Cdk1 *in vitro*.

(D) Fractions from size-exclusion chromatography of Cik1-Kar3 and Bim1. Top gel shows that Bim1 co-elutes with Cik1-Kar3 indicating a robust interaction between the molecules when Cik1-Kar3 was dephosphorylated by lambda phosphatase. Lack of co-elution in the bottom gel shows a weakened interaction after Cik1-Kar3 was phosphorylated by Cdc28/Cdk1.

**Figure 3. Mal3 and Cik1-Kar3 constitute a minimal system that converts growth of microtubules from a common MTOC into formation of parallel microtubule bundles**

(A) Scheme of the experimental setup. Microtubules are grown from *Tetrahymena* pellicles immobilized on coverslips. All microtubule plus-ends are pointing away from the pellicles. Arrows indicate direction of Cik1-Kar3 movement.

(B)-(D) Imaging of Mal3 (green) and Cik1-Kar3 (red) on microtubules growing from *Tetrahymena* pellicles. Top: schematic representations. White arrows indicate direction of the molecule movement. Bottom: Kymograph. Plus (+) and minus (-) denote microtubule polarity. (B) Only Cik1-Kar3 is present. (C) Only Mal3 is present. (D) Both Mal3 and Cik1-Kar3 are present.

(E) Time sequence of Mal3 images in Mal3+Cik1-Kar3 (top) and Mal3 only (bottom) experiments. Rightmost panels are schematic representations of the last frames of the sequence. Blue arrows indicate tips of microtubules that grow in independent directions. Red arrows indicate tips of guided microtubules.

(F) Flowchart of the automated pipeline used for the processing of the *in vitro* imaging data.

(G) Fraction of microtubules whose growth is guided along others. Dotted line indicates theoretical fraction of guided microtubules for the given density of nucleation centers and microtubule dynamics instability parameters (see Figure S3). Error bars are SEM.

(H) Histograms of Cik1-Kar3 fluorescence signal intensity at the tips of the guided (red) and independent (blue) microtubules.

(I) Microtubule growth rates of guided microtubules as a function of the intensity of Cik1-Kar3 fluorescence signal at their tips. Weak motor affinity of Cik1-Kar3 data (gray) is obtained at 1 mM ADP, normal motor affinity (red) at 1 mM ATP. Error bars are SEM.

(J) Imaging of Mal3 (green) and phosphorylated Cik1-Kar3 (red) on microtubules growing from Tetrahymena pellicles. Top: schematic representations. Bottom: Kymographs.

**Figure 4. Cik1-Kar3 is a weak motor that makes frequent backward steps**

(A) Scheme of the optical trapping setup.

(B) Fraction of moving beads as a function of kinesin concentration. The data are well fitted with Poisson distribution assuming that one kinesin is sufficient to move the bead ( $n \geq 1$ , blue,  $\chi^2 = 0.38$ ). Assuming that two or more kinesins are required to move the bead leads to a less well fit ( $n \geq 2$ , red,  $\chi^2 = 4.63$ ). Error bars are SEM.

(C) Force-velocity relationship at 6 mM ATP. Trap stiffness was 0.0035 pN/nm. The solid line shows a linear fit. Error bars are SEM.

(D) High resolution recordings of individual Cik1-Kar3 kinesin moving in an optical trap at saturating ATP concentrations. Two independent traces from different experiments are shown. Data were acquired at 4 kHz and median-filtered with a window width of 25 ms. Red line is the fit to a step function used to extract magnitude of steps.

(E) Distribution of the step sizes from single molecule traces extracted at 6 mM ATP.

(F) ATP concentration dependence of the velocity of Cik1-Kar3 movement. Solid line is the hyperbolic fit with  $K_m = 0.25 \pm 0.15$  mM. Data is shown as black circles and error bars are SEM.

(G)-(H) Number of events as a function of dwell time for high (6 mM) and low (6  $\mu$ M) ATP. Solid lines are exponential fits. Average dwell times are shown in upper top part of the graph.

(I) Recording of the position of the bead at 6  $\mu\text{M}$  ATP. The trace shows several back steps induced by the opposing force.

(J) Distribution of the step sizes under the opposing force at 6  $\mu\text{M}$  ATP. Solid line is the fit to the sum of Gaussian functions, which yields position of the peaks at  $-16 \pm 0.87$  nm,  $-8.1 \pm 0.186$  nm, and  $7.97 \pm 0.55$  nm (errors are 95% confidence intervals).

**Figure 5. Minus-end directed movement of Cik1-Kar3 is driven by the difference between asymmetries of the binding potential in no NTP and ATP states**

(A) A recording from the experiment in which lifetimes under external force are measured. Positive force is directed towards the plus-end of the microtubule.  $\tau_1$  and  $\tau_2$  are lifetimes for the kinesin under the force directed towards minus-end and plus-end, respectively.

(B), (C) Dependence of the detachment lifetime on the applied force for wt Cik1-Kar3 in no NTP and AMPPNP states. Solid lines are fits to the Equation 1. Blue points represent individual measurements (n=280).

(D) A model depicting parameters that describe asymmetric binding potential and the change of the off rate constants as a function of the applied force.

(E), (F) Dependence of the detachment lifetime on the applied force for Cik1<sup>(1-360)</sup>-Kar3 mutant in no NTP and AMPPNP states. Solid lines are fits to the Equation 1.

**Figure 6. Plus-end guiding activity of *Drosophila* and human kinesin-14 Ncd and HSET lead to parallel microtubule growth**

(A), (B) Images of *Drosophila* EB1 (dmEB1) and Ncd on microtubules growing from Tetrahymena pellicles at 50 mM (A) and 100 mM (B) KCl. Top: schematic representations. Bottom: Kymographs of dmEB1 (green) and Ncd (red). Plus (+) and minus (-) denote microtubule polarity. At increased salt concentrations (B) Ncd localizes primarily to microtubule tips and promotes parallel microtubule growth.

(C) Comparison of the fraction of guided microtubules in the presence of *Drosophila* and human EB1 and presence or absence of *Drosophila* or human kinesin-14 (Ncd, n=252 or HSET, n=90). For both *Drosophila* and human protein pairs presence of kinesin-14 statistically significantly increases microtubule bundle formation by guided growth at 95% significance level.

(D) Images of human EB1 (hsEB1) and kinesin-14 (HSET) on microtubules growing from Tetrahymena pellicles. Nomenclature follows (A).

(E) A static image of prometaphase S2 cell expressing EB1-GFP.

(F) Kymograph of astral microtubules from S2 cell shows multiple EB1 ends indicating growth of a parallel microtubule bundle.

(G) Comparison of the fraction of guided astral and spindle microtubules for control (n=118, astral; n=98, spindle) and Ncd RNAi cells (n=120, astral; n=127, spindle). Error bars are SEM.

**Figure 7. Mechanism for the formation of parallel microtubule bundles by EB1 and kinesin-14**

(A)-(D) The multi-step mechanism takes advantage of the intrinsic ability of the motor to move to the minus ends of microtubules (A), where it can engage with newly growing plus-ends (B) and

guide their growth in plus-end direction (C). Bundling is controlled by phosphorylation (D). When yeast kinesin-14 Cik1-Kar3 is phosphorylated by Cdc28/Cdk1, it does not interact with EB1 allowing microtubules to grow in all directions, maximally exploring space. Top panels illustrate mechanistic events at the level of single kinesin molecules for each step of the microtubule bundling process. Bent arrows indicate probabilities of making forward and reverse steps, and  $k_{,+}^{(step)}$  - denote stepping rates towards the plus and minus ends, respectively.

(E) Addition of EB1/kinesin-14 to microtubules growing from an MOTC leads to the formation of bundles that are oriented in random directions. Selective stabilization of microtubule dynamics towards the shmoo tip is sufficient to provide the direction for the formation of the bundle.

(F) Theoretical probabilities based on simulations that a single microtubule bundle points to the shmoo tip when microtubules are spatially stabilized towards one direction, and when no stabilization exists, i.e. all directions are equal. For details, see Methods.

## SUPPLEMENTAL FIGURE LEGENDS

### Figure S1. Characterization of the Bim1-Mal3 chimera. Related to Figure 3.

(A) Kymograph of TIRF images showing the behavior of Bim1 on a dynamic microtubule at 50 mM KCl. The strong interaction of Bim1 with the lattice of the microtubule obscures the tip tracking.

(B) The engineered chimeric EB1 protein consists of residues 1-178 of Mal3, which include CH domains and the linker and residues 194-344 of Bim1.

(C) Kymographs of TIRF images showing behavior of chimeric EB1 (green) and Cik1-Kar3 (red) on microtubules growing from *Tetrahymena* pellicles. Plus (+) and minus (-) denote microtubule polarity.

(D) Fraction of microtubules whose growth is guided along template microtubules in the presence of chimeric EB1 in the absence and presence of Cik1-Kar3. Fraction of guided microtubules in the presence of the chimera is indistinguishable from the fraction of guided microtubules in the presence of Mal3 protein (Figure 3G).

(E) Serial dilution growth assay of the indicated yeast strains at 37°C show that integration of the Mal3-Bim1 chimera improves the compromised growth of a *bim1* deletion at 37°C.

(F) Maximum intensity projection images of yeast cells expressing GFP-tagged Mal3-Bim1 chimera in alpha factor arrested and cycling cells. Arrows indicate the localization to microtubule plus ends and the spindle midzone. Scale bar is 2  $\mu$ m.

**Figure S2. Characterization of Cik1-Kar3 plus-end guiding *in vitro*. Related to Figure 3.**

(A)-(B) Histograms showing number of microtubule tips growing within the same bundle in the presence (A), (n=950 microtubules) and absence (B) of Cik1-Kar3 (n=330 microtubules).

(C) Microtubule growth rate in the absence of Mal3 does not depend on Cik1-Kar3 (n=60 microtubules). Error bars are SEM.

(D) Kymographs of TIRF images showing behavior of Mal3 (green) and Cik1-Kar3 (red) in the presence of 1 mM ADP; Cik1-Kar3 binds microtubules weakly and occasionally diffuses along the lattice.

(E) Kymographs of TIRF images showing behavior of Mal3 (green) and Cik1-Kar3 (red) in the absence of the nucleotide. Cik1-Kar3 binds microtubules tightly and doesn't move along the lattice. Plus (+) and minus (-) denote microtubule polarity.

**Figure S3. Simulation of the microtubule dynamics and bundling. Related to Figure 3.**

(A) Microtubules (arrows) are nucleated at nucleation centers (circles). Positions of nucleation centers  $(x_i, y_i)$ , directions of microtubules  $(n_i)$  and microtubule dynamics are extracted from experimental data in the absence of Cik1-Kar3 (Movie S1) and fully define the model. Plus-ends of microtubules are indicated.

(B) In the presence of Cik1-Kar3 the end of the microtubule (k) is captured by a template microtubule (i) when it approaches it within 100 nm region (shown as dotted circle). Following this event, growth of microtubule (k) is guided along microtubule (i), which leads to the change in the

direction of growth shown as change in the angle  $\alpha$ . Microtubule (k) is then classified as guided and (k) as independent.

(C) Simulated fraction of guided microtubules growing from pellicles as a function of microtubule catastrophe rate. Density of nucleation centers was  $1 \mu\text{m}^{-2}$ . Simulation is shown as the solid line. Experimental parameters are shown as the black data point with error bars. Error bars denote SEM.

(D) Simulated fraction of guided microtubules growing from pellicles as a function of density of microtubule nucleation centers in the pellicle. Catastrophe rate was  $0.007 \text{ sec}^{-1}$ . Simulation is shown as the solid lines. Experimental parameters are shown as the black data point with error bars. Error bars denote SEM.

(E) Simulated fraction of guided microtubules as a function of time for a single simulation is shown for parameters corresponding to the catastrophe rate  $0.007 \text{ sec}^{-1}$  and density of nucleation centers  $1 \mu\text{m}^{-2}$ . The simulation starts with all microtubule lengths set to zero and no guided microtubules. As microtubules start to grow, some become guided and the fraction reaches steady state indicated by dotted line. Its y-value is then taken as fraction of guided microtubules for a given set of parameters.

**Figure S4. Cik1-Kar3 associated with growing microtubule tips can guide growth towards both plus and minus ends. Related to Figure 3.**

(A) Scheme of the *in vitro* guiding assay. Microtubules are grown from biotinylated GMPCPP seeds immobilized on Avidin coated coverslips. Polarity of microtubules is identified by the natural

minus-end direction of the lattice bound Cik1-Kar3 movement. A fraction of Cik1-Kar3 localizes to the microtubule tip via the interaction with Mal3. When the tip of a guided MT encounters the lattice of a template MT, tip bound Cik1-Kar3 might guide growth either toward the plus or to the minus end depending on the encounter angle (shown).

(B) Time sequence for a typical example of the guiding towards the minus end is shown for the encounter angle of 140 degrees. Top are Mal3 images, bottom are schematic representations of the top images. Red arrow points to the plus end of the guided microtubule.

(C) Time sequence for a typical example of the guiding towards the plus end is shown for the encounter angle of 22 degrees. Top are Mal3 images, bottom are schematic representations of the top images. Red arrow points to the plus end of the guided microtubule.

(D) Quantification of the occurrence of guiding events towards plus and minus ends as a function of the encounter angle. Not guided microtubules are events in which guided tip either crossed the template microtubule or underwent a catastrophe and no guiding occurred. Mal3 concentration was 160 nM, Cik1-Kar3 concentration was 10 nM (n = 242 events).

**Figure S5. Characterization of the optical trapping methodology and single-molecule properties of Cik1-Kar3 movement. Related to Figures 4 and 5.**

(A) Schematic of the experimental setup. W1, W2 - wave plates; PBS - Polarizing cube beam-splitter; PM - Piezo mirror; ND - neutral density filters; D1-D3 dichroic mirrors; QPD - quadrant photo-detector.

(B) The graphs show QPD signals (X and Y) for different bead positions in the x,y plane. The bead was trapped  $\sim 100$  nm above the coverslip and moved across the detector beam from  $-1 \mu\text{m}$  to  $1 \mu\text{m}$  in x,y with 50 nm steps using a piezo-mirror. In the area shown with dotted circle function of the QPD voltage is single valued. It was fitted with 5<sup>th</sup> order 2 dimensional polynomial and used as a calibration for the position detection.

(C) The graph shows unprocessed recording from a single  $0.28 \mu\text{m}$  size bead held at the microtubule surface in the presence of 6mM ATP, and it shows multiple runs of the kinesin. Trap stiffness was 0.0035 pN/nm.

(D)-(E) Number of single-molecule events as a function of run length of unloaded Cik1-Kar3 at 6 mM (D) and  $6 \mu\text{M}$  (E) ATP. Solid line is an exponential fit, and average run-length is indicated at the top right corner of the graph.

(F) Number of single-molecule events as a function of run length of Cik1-Kar3 at  $6 \mu\text{M}$  ATP moving towards the plus-end at an average load of 0.3 pN. Solid line is exponential fit with average run-length value indicated in the top right corner of the graph.

(G) Top: bright-field/fluorescence image of the  $1 \mu\text{m}$  size bead and segmented microtubule. Bottom: Schematic representation of the top image. (+) and (-) indicate plus- and minus-ends of the microtubule. x and y indicate axes of the position detector,  $\alpha$  is the tilt of the microtubule with respect to the x detector axis.

(H) Unprocessed X and Y recordings of the lifetime measurement when force was applied in 3 consecutive steps towards the plus end of the microtubule.

(I) Same data as in (E) but axes were rotated at angle  $\alpha$ , in order to extract position of the bead along the microtubule, which is used for further processing.

**Figure S6. Brownian ratchet model of Cik1-Kar3 movement. Related to Figure 5.**

(A) In no NTP state Cik1-Kar3 undergoes bound diffusion (indicated by arrows) and makes more distant excursions towards the minus end due to the asymmetry of the binding potential (shown on the right). Opposing external force (red arrow) biases the movement towards the plus-end. Relative occupancy of the Cik1-Kar3 positions along the microtubule is shown as number of molecules on the potential energy plot in (A)-(E).

(B) Binding of ATP can rectify movement of Cik1-Kar3 in no NTP state when it traveled further than  $\Delta$  upon ATP binding due to the associated change of the potential energy landscape (shown on the right), which propels the molecule to the next potential minimum towards the minus end. In other cases, binding of ATP does not lead to the productive movement.

(C) After ATP hydrolysis, Cik1-Kar3 enters freely diffusing state. Presence of the external force (red) biases this movement towards the direction of the force.

(D) Mutant Cik1-Kar3 that lacks motor-homology domain is bound via the symmetric potential (right) and therefore does not have any preference in minus or plus end directed thermal movements.

(E) Binding of ATP can rectify plus- and minus- end directed excursions of  $\Delta$ Cik1-MHD in no NTP state with equal probability due to symmetry of the binding potential. This leads to a step that is equally likely to be plus or minus end directed.

(F) After ATP hydrolysis  $\Delta$ Cik1-MHD enters a diffusive state similar to the wild type.

**Figure S7. ATPase activity of full length Cik1-Kar3. Related to Figures 4 and 5.**

(A),(B) Cik1-Kar3 displays a maximal ATPase rate ( $k_{\text{cat}}$ ) of  $14.8 \pm 1 \text{ sec}^{-1}$ , and a  $K_m$  (microtubules) of  $0.6 \pm 0.2 \text{ }\mu\text{M}$  and  $K_m$  (ATP) of  $0.16 \pm 0.03 \text{ mM ATP}$ . The ATPase rate is expressed as Pi released/sec/motor. Each point represents the mean  $\pm$  SEM.

**SUPPLEMENTAL TABLE LEGENDS**

**Table S1.** Parameters of the interaction potentials between Cik1-Kar3 and microtubule lattice for wt and mutant molecules in no NTP and AMPPNP states. Errors are 95% confidence intervals. Related to Figure 5.

**SUPPLEMENTAL MOVIE LEGENDS**

**Movie S1.** Microtubules growing from a common nucleation center (pellicle) in the presence of Mal3. Mal3 is shown in yellow; the microtubules are shown in red. Data was collected at 1 frame/s. Mal3 concentration was 160 nM. Images were background subtracted.

**Movie S2.** Microtubules growing from a common nucleation center (pellicle) in the presence of Mal3 and Cik1-Kar3. Mal3 is shown in yellow; the microtubules are shown in red; no Cik1-Kar3 channel is shown. Data was collected at 0.65 frame/s. Mal3 concentration was 160 nM, Cik1-Kar3 concentration 20 nM. Images were background subtracted.

**Movie S3.** Simulation of microtubules growing from a common nucleation center in the presence of EB1. Microtubule tips are yellow and microtubules are red. Parameters of nucleation density centers and microtubule dynamics are the same as in Movie S1.

**Movie S4.** Simulation of microtubules growing from a common nucleation center in the presence of EB1 and Cik1-Kar3. Microtubule tips are yellow and microtubules are red. Cik1-Kar3 is assumed to present at all microtubule tips and is not shown. Parameters of nucleation density centers and microtubule dynamics are the same as in Movies S1 and S3.

**Movie S5.** Simulation of microtubules growing from a SPB in mating yeast cells. Bundling is due to EB1/Cik1-Kar3. Microtubules that reach shmoo tip are stabilized (see Supplemental Information for details). Cell and nucleus shapes are outlined in white. Microtubules are red. Microtubule ends are yellow.

**Movie S6.** Simulation of microtubules growing from a SPB in mating yeast cells. Bundling is due to EB1/Cik1-Kar3. No additional microtubule stabilization at the tips was assumed and all directions are equal. Cell and nucleus shapes are outlined in white. Microtubules are red. Microtubule ends are yellow.

## **STAR METHODS TEXT**

### **CONTACT FOR REAGENT AND RESOURCE SHARING**

Further information and requests for reagents may be directed to, and will be fulfilled by the corresponding authors Stefan Westermann ([stefan.westermann@uni-due.de](mailto:stefan.westermann@uni-due.de)) or Alipasha Vaziri ([vaziri@rockefeller.edu](mailto:vaziri@rockefeller.edu))

### **EXPERIMENTAL MODEL AND SUBJECT DETAILS**

#### **Yeasts**

All yeast strains are derived from the S288C wildtype strain (ATCC) and were genetically modified using standard procedures.

#### **Tetrahymena**

A mucus-free strain of Tetrahymena (SB255) was obtained from Cornell University Tetrahymena Stock Center. Cells were kept in anaerobic soybean stocks. Before purification, media was inoculated with ~ 500 µl of the stock and grown overnight at 30 degrees. Next day 1 ml of the culture was used to inoculate 20 ml of the media and grown overnight. Next day 200 ml culture was inoculated in 2 L flasks and grown until mid-log phase at 30 degrees. This yielded enough cells for ~ 100 assays.

#### **Insect cell culture**

Sf9 cells were purchased from ThermoScientific and were cultured according to the manufacturer's instructions using Grace's Insect Cell Media supplemented with 10% FBS, 100 U/ml Penicillin, 0,1 mg/ml Streptomycin, 2 mM L-Glutamine and 0,1% Pluronic® F-68. Transfection was done with Eugene6 Transfection Reagent (Promega). Virus amplification and protein expression was performed according to the instructions of ThermoScientific.

## **Drosophila**

Commercial S2 were obtained from ThermoFisher Scientific and cultured in Schneider media (Sigma S0146) with 10% FBS (Sigma F9665) and 1% Penicillin/Streptomycin (Gibco 15070-063). To maintain the S2 culture, cells were split every 3-4 days at ratio 1:5. To make stable cell lines expressing EB1-GFP under the inducible metallothionein promoter (plasmid gift from Gohta Goshima) we plated ~ approximately 350,000 S2 cells in 24-well plates for 2 hours in 900µl of full media. 30 minutes before transfection 0.6µg vector DNA was mixed with 0.06µg pCoBlast (Invitrogen), 1µl Transit-Insect (Mirus Bio) and 100µl Serum free Schneider medium (SFM). The medium of the plated S2 cells was removed and the transfection mix was added. After 3-4 hours 1ml Serum containing Schneider medium was added. Cells were incubated for 4 days before adding 25µg/ml Blastocidin (Invitrogen). After 1-2 weeks stable cultures were obtained. GFP-expression was analysed by immunofluorescence.

## **METHOD DETAILS**

### **Live cell imaging of yeast cells**

Fusions of fluorophores to yeast genes were introduced into the S288C background. To image the mating projection log-phase yeast cells were synchronized in G1 with  $\alpha$ -factor (10  $\mu$ g/ml) for 120-135 min in synthetic medium supplemented with 2% glucose. These cells were adhered on coverslips via Concanavalin A coating, sealed and immediately imaged using a live cell DeltaVision (Applied Precision) microscope equipped with an UPlanSApo x 100-oil immersion objective lens (Olympus) and a Coolsnap HQ CCD camera (Photometrics).

Each image consists of 7 z-stacks with planes 0.25  $\mu$ m apart. Time-lapse movies were acquired every 5 s. Planes were projected to two-dimensional images using SoftWoRx (DeltaVision) and further processed using ImageJ and using software custom made in MATLAB (MathWorks).

Fraction of microtubules growing along the bundle was quantified by scoring all microtubules, whose growth was clearly visible and classifying whether the growth was guided along the shmoo tip by eye.

### **Protein Biochemistry**

Purification of the kinesin-14 motor complexes was done as described before (Mieck et al., 2015) with some modifications. Full-length Cik1-Kar3 protein coding sequences were amplified from yeast genomic DNA and cloned into the two cassettes of the pFastBacDual plasmid (Life Technologies) for co-expression in SF9 insect cells. Cik1's C-terminus was fused to a 1xFLAG tag and Kar3 was untagged or modified N-terminally by a HaloTag (DHA, Promega). The protein was expressed according to the manufacturer's manual. Cell lysis was achieved by resuspending the insect cell pellets in lysis buffer (25 mM Hepes pH 7.4, 1 mM MgCl<sub>2</sub>, 0.1 mM EGTA, 0.5 mM EDTA, 0.1% Tween-20, 5% glycerol, 300 mM NaCl, 0.5 mM ATP, 1 mM PMSF, PhosSTOP Phosphatase Inhibitor Cocktail (Roche)) and homogenized by 10 strokes using a douncer. After centrifugation at

30.000 x g for 20 min the supernatant was incubated with pre-washed M2 affinity agarose (Sigma-Aldrich) for 1 hour at 4°C. After five washes elution was performed by adding one resin volume of elution buffer (lysis buffer adjusted to 2mg/ml 3xFLAG peptide, 250 mM NaCl, 1 mM DTT, omitting ATP and PhosSTOP) to the agarose. If further purification steps were required, the heterodimeric motor was loaded onto a cation exchange chromatography (MonoS 5/50 GL, GE Healthcare). For the fluorescent labeling Kar3 bound to M2 agarose was incubated with HaloTag TMR ligand (Promega) at 4 degrees for 2 hours. Extensive washing removed unbound TMR ligand and the kinesin was eluted as described above.

The Mal3 expression construct was kindly provided by T. Surrey. In order to create a chimeric protein, Mal3 fragment 1-178 (amino acid residues) and Bim1 fragment 194-344 were fused together. The two fragments were cloned as NheI-BamHI and BamHI-NotI fragments and ligated into plasmid pet28a. Bim1, Mal3 and Bim1-Mal3 chimera were all expressed in E. coli BL21 and purified using Ni-NTA column in buffer A (25 mM sodium phosphate with pH 7.5, 400 mM NaCl) containing 15 mM imidazole. Proteins were eluted in buffer A containing 200 mM imidazole, desalted and labeled with Alexa 488 dye by incubating for 1 hour with Alexa Fluor 488 FTP ester at room temperature. Proteins were further purified from unbound dye on the Superose 6 size exclusion column and the tag was cleaved off overnight by either TEV protease or Thrombine at 4°C.

Cdc28-Clb2 kinase complex was overexpressed from a galactose promoter and affinity purified via Clb2-TAP. The yeast pellet was homogenized using a freezer mill, lysed in Buffer A (50 mM bis-Tris propane pH 7.0, 100 mM KCl, 5 mM EGTA, 5 mM EDTA, 10% glycerol and 1% Triton X-100) and incubated with IgG sepharose slurry. Beads were washed with Buffer A adjusted to 300 mM KCl

and subsequently with TEV cleavage buffer (25 mM Tris-HCl pH 8.0, 150 mM NaCl, 0.1 % NP-40, 0.5 mM EDTA, 1mM DTT). TEV was added and cleaved overnight at 4 degrees. Afterwards 3 volumes of Calmodulin-binding Buffer (25 mM Tris-Hcl pH 8.0, 150 mM NaCl, 0.02% NP-40, 1mM MgCl<sub>2</sub>, 1 mM Imidazole, 2 mM CaCl<sub>2</sub>, 1mM DTT) were added to the TEV cleaved sample together with calmodulin sepharose 4B slurry. Beads were washed with Calmodulin-binding Buffer and eluted with 20 mM EGTA.

Genes encoding *Drosophila* EB1 and Ncd were a kind gift from G. Goshima. dmEB1-GFP was cloned into pET28 vector, expressed in BL21 cells, purified using Ni-NTA in buffer containing 50 mM sodium phosphate pH 6.8, 2mM MgCl<sub>2</sub>, 400 mM NaCl and 15 mM Imidazole and run on Superose 6 gel filtration column.

Ncd was cloned into pFastBac with N terminal his-tag and C terminal HALO tag. The protein was expressing in Sf9 insect cells, and purified using Ni-NTA in buffer containing 25mM HEPES pH 7.5, 1mM MgCl<sub>2</sub>, 300 mM NaCl, 10% glycerol, 0.1% Tween-20, 0.1 mM ATP, 10 mM βME, 0.1 mM EGTA, 0.1 mM EDTA, and 20 mM Imidazole. The protein was labeled with TMR-Halo ligand and eluted in the buffer containing 250 mM Imidazole. His-tag was cleaved off overnight at 4°C with 0.02 mg/ml TEV.

Human EB1 expression plasmid was a kind gift from T. Kapoor. YBBR tag was cloned at the C terminus of EB1, and the protein was expressing in BL21 RIL cells. hsEB1-YBBR was purified using Ni-NTA in the buffer containing 50mM sodium phosphate pH 7.2, 400 mM NaCl and 15 mM Imidazole. The protein was desalted and coupled to CoA-Alexa-595 dye using 10 uM SFP overnight. His-tag was cleaved off overnight at 4°C with 0.02 mg/ml TEV.

HSET-GFP in pFastBac was a kind gift from C. Walczak. The protein was expressed in Sf9 insect cells. Cells were lysed by 10 strokes of glass homogenizer in buffer containing (80 mM Pipes, pH 6.8, 1 mM MgCl<sub>2</sub>, 1 mM EGTA, 0.1 mM EDTA, 100 mM NaCl, 1 mM DTT, 2 mM ATP) and protease inhibitors. After clarification at 12000 rpm for 15 min the supernatant was filtered through a 0.2 μm filter, loaded on a 1 ml HiTrap<sup>TM</sup> SP column equilibrated in (20 mM Pipes, pH 6.8, 1 mM MgCl<sub>2</sub>, 1 mM EGTA, 0.1 mM EDTA, 100 mM NaCl, 1 mM DTT, 50 mM ATP) and eluted with a linear 100–500 mM NaCl gradient. Peak XCK2 fractions were concentrated and then further purified on a Superose 6 gel filtration column.

### **Kinase assay**

Purified motor constructs were incubated with Cdc28-Clb2 purified from yeast and γ-[<sup>32</sup>P]ATP in Cdk1 buffer (25 mM Hepes pH 7.6, 100 mM KCl, 2 mM MgCl<sub>2</sub>, 1 mM DTT, 1mM EGTA, 5% glycerol, 20 mM β-glycerophosphate) for 30 min at 30°C. SDS PAGE and exposure to an autoradiography film (Kodak) visualized the phosphorylation state of the motor. For mass spectrometry analysis of the in vitro phosphorylated motors, the respective sample was dephosphorylated prior to the kinase assay using lambda phosphatase (NEB).

### **Size exclusion chromatography**

The interaction studies of Kar3-Cik1, Bim1 and Cdc28-Clb2 were conducted on a Superose 6 column (GE Healthcare) at 4°C under the following conditions: 25 mM Hepes (pH 7.4), 250 mM NaCl, 1 mM MgCl<sub>2</sub>, 0.1 mM EGTA, 0.1 mM EDTA, 1 mM DTT, 1 mM ATP. Protein elution was

monitored by absorbance (wavelength of 280 nm) and the elution fractions were analyzed by SDS-PAGE and subsequent Coomassie staining.

### **Cross-linking / Mass spectrometry**

To set up the cross-linking reactions 3.3  $\mu\text{M}$  Cik1/Kar3 was treated separately or mixed together with 3.3  $\mu\text{M}$  Bim1. These samples were incubated with varying concentrations of the cross-linker bis(sulphosuccinimidyl)suberate BS3 (100-600  $\mu\text{M}$ ) in the presence of 200 mM NaCl for 20 min. The reaction was quenched by addition of ammonium bicarbonate and incubation for 10 min at ambient temperature. An aliquot of the reaction was analyzed by SDS PAGE and the chosen samples were digested using trypsin following a standard protocol.

After digestion and prior to LC-MS/MS measurement samples were purified on Super SW2000 column. The fractions containing the crosslinked peptides were evaporated to dryness, resuspended in 10-50  $\mu\text{L}$  of 0.1% TFA and measured using UltiMate 3000 HPLC RSLC nano system coupled to a Q-Exactive plus mass spectrometer (Thermo Fisher Scientific) with a Proxeon nanospray source. Peptides were separated using a flow rate of 275 nL/min and the following gradient: 0-10 min: 2% B, 10-130 min: to 35% B, 130-135 min: to 90% B, 135-140 min: 90% B, 145-142 min: to 2% B, 142-165: 2% B. The mass spectrometer was operated in data-dependent mode (recording from 20-160 min of the LC method), selecting up to 12 precursor ions from MS1 scan (resolution = 70000) in the range of  $m/z$  350-2000 for higher-energy collisional dissociation (HCD). Fragment ions were analyzed with resolution set to 17 500 and an ion threshold of  $5e4$  excluding singly and doubly charged ions. HCD was performed with 28% normalized collision energy, an isolation window of 1.6  $m/z$  and a fixed first mass of 150  $m/z$ . The underfill ratio was set to 10%,

dynamic exclusion to 30 s and peptide match was switched off. Ion target values were  $1e6$  (maximum injection: 60 ms) for full scans and  $5e4$  (maximum injection: 500 ms) for MS/MS scans.

### ***In vitro* reconstitution of microtubule bundle formation**

To isolate tetrahymena pellicles 400 ml of tetrahymena cells were grown until mid-log phase. Cells were washed with fresh medium and resuspended in ~ 50 of cold PME buffer (80mM PIPES, pH 6.9, 2mM  $MgCl_2$ , 1 mM EGTA) plus protease inhibitors. After two additional washed cells were resuspended in ~ 10 ml of the PME buffer plus inhibitors containing 0.25% of the NP-40 alternative and mechanically deciliated with a single one-second stroke of Polytron pt 10/35 homogenizer. Pellicles were washed three times with PME plus proteins inhibitors to get rid of the detergent, the final pellet was resuspended in three volumes, aliquoted and frozen in liquid nitrogen.

Before the assay, pellicles were adhered to hydrophobic coverslips silanized with dichlorodimethylsilane (Sigma). Afterwards the surface was blocked with Pluronic F-127 to prevent unspecific binding. Dynamics of Mal3 and Cik1-Kar3 on microtubules was observed on a commercial TIRF microscope (Zeiss). Unless stated otherwise a mixture containing 1.9 mg/ml tubulin, 160 nM EB1 and 20 nM Cik1-Kar3 was added to the flow cell in assay buffer (100mM K-PIPES pH 6.8, 20 mM KCl, 4mM  $MgCl_2$ , 1mM GTP, 1mM EGTA, 10mM 2-mercaptoethanol and 1mM ATP and 0.5 mg/ml  $\beta$ -casein) and an oxygen scavenger system. For experiments in different nucleotide states ATP was replaced with 1 mM ADP, 1 mM AMPPNP or 5 units/ml Apyrase (NEB). The protein concentrations were chosen after systematic variation of concentrations to allow the easy visualization of both end tracking and transport along microtubules. The temperature was 34 °C.

Experiments with *Drosophila* and human EB1 and kinesin-14 were done using the same protocol. Additionally KCl was added to 50 or 100 mM final concentration. For the experiments with *Drosophila* proteins, flow cell assay buffer (see above) was supplemented with 1.9 mg/ml tubulin, 500 nM dmEB1-GFP and 50 nM Ncd-TMR. For the experiments with human proteins, flow cell assay buffer was supplemented with 1.9 mg/ml tubulin, 1  $\mu$ M hsEB1-Alexa594 and 50 nM HSET-GFP. For the experiments with human proteins, the temperature was 37 °C.

### **Optical trapping instrumentation**

All measurements were performed on custom-made optical tweezers (Figure S5A) (Grishchuk et al., 2005). Briefly, 1064 nm laser (MANLIGHT) was coupled into the Olympus IX71 inverted microscope with 100x NA1.3 oil immersion objective, which was extensively modified for improved stability (Lang et al., 2002). Position of the trap in the sample was controlled with Nano-MTA piezo mirror (Mad City Labs). An independent laser iFLEX2000 (Qioptiq) was used for tracking the position of the bead on the quadrant photodiode (QPD) (SPOT-9DMI, OSI optoelectronics) with custom-made low noise electronics. NA 1.4 condenser was used to collect the light after interaction with the bead and focus it with an additional achromatic lens on the QPD. Position of the specimen was controlled by three-axis piezo stage Nano-LPQ (Mad City Labs).

Calibration of the QPD was obtained by scanning the trapping beam across the tracking laser in 2D using piezo mirror (Figure S5B). Trap stiffness was measured by hydrodynamic drag measurement and confirmed by power spectral analysis (Lang et al., 2002). Data was hardware anti-alias filtered at 100 kHz, sampled at 200 kHz and further software low-pass filtered and down-sampled to 4kHz. For further processing data was additionally smoothed by sliding average.

### **Preparation of the sample for optical trapping**

Carboxyl modified polystyrene beads were purchased from Bang Labs. 0.28  $\mu\text{m}$  size beads were used for high resolution stepping experiments, and 1  $\mu\text{m}$  size beads were used in potential energy landscape measurements in no NTP and AMPPNP states. The coating procedure for both types was the same. Anti-HALO antibody (Promega) was coupled to the beads via a two-step procedure. Carboxyl groups were activated using EDC and sulfo-NHS. The activated carboxyl groups reacted with amine groups of the PEG mixture (2kDa, Rapp Polymere, Germany), 95% of which consisted of nonreactive methylated PEGs, and 5% of PEG that possessed non-activated carboxyl group. These carboxyl groups at the other end of the PEGs were activated by a second reaction identical to the first activation. The Anti-HALO antibodies reacted with the activated carboxyl groups of the PEGs. The microspheres were stored in PBS buffer supplemented with 0.1 mg/ml BSA and used for no longer than 2 weeks. Before each experiment full length Cik1-Kar3(HALO) was mixed with beads at equal volumes and incubated for 10 min at room temperature.

Microtubules were polymerized from unlabeled porcine tubulin (purified from porcine brains) and TRITC porcine tubulin (cytoskeleton) at 20:1 ratio and stabilized by taxol. Segmented microtubules with longer fragments at plus ends were made by first polymerizing bright GMPCPP seeds containing 1:3 of rhodamine tubulin for 15 min in the presence of 0.5 mM GMPCPP. Seeds were then added to the tubulin/GTP mixture at 1:15 ratio and polymerized for another 20 minutes after which taxol was added stepwise up to 10  $\mu\text{M}$ . Microtubules were adhered to coverslips by anti-beta-tubulin antibodies (Sigma) and the surface was blocked by Pluronic F127 (Sigma). Mixture of kinesin-coated beads was then added to the chamber in the assay buffer (100mM PIPES pH 6.9, 1

mM MgCl<sub>2</sub>, 1mM EGTA, 0.5 mg/ml β-casein, anti-scavenging mix: glucose oxidase 0.2mg/ml, catalase 0.035 mg/ml, glucose 25mM, and βME 70mM), and the chamber was sealed. Beads and microtubules were visualized on the EMCCD simultaneously by combination of 561 nm wavelength laser, which excited fluorescence of microtubules, and weak transmission light that made beads visible. A bead was caught in the optical trap and then brought to the microtubule to test its binding. Axial distance from the bead to the microtubule was probed by raising the piezo stage until sum signal on QPD began to change indicating the bead contacted the glass surface. After that, the bead was positioned 0 – 100 nm above the microtubule and the position of the bead was recorded in the stationary trap for up to 3 min. A typical dilution of kinesin was 1:10000 – 1:50000 from original purification stock (~ 6 μM) and was chosen such that less than 40% of beads showed motility.

### Measurement of force-velocity curves

Force-velocity was measured in fixed position optical trap by linear regressions of position traces as a function of force. Since individual kinesin attached to the bead has certain compliance, velocity of the kinesin is related to the velocity of the bead by factor  $k_{kin}/(k_{kin}+k_{trap})$ , where  $k_{trap}$  is the trap stiffness and  $k_{kin}$  is the stiffness of the kinesin molecule (Svoboda and Block, 1994). We measured stiffness of Cik1-Kar3 by moving the piezo stage at a known rate, while holding the bead with a single kinesin attached to the microtubule in a rigor-like state. This resulted in the  $k_{kin} = 0.03 \pm 0.004$  pN/nm for the full length Cik1-Kar3 attached to the bead. This value was used together with trap stiffness, which typically was 0.0035 pN/nm in these experiments in order to extract velocity of the kinesin from the velocity of the bead.

### **Lifetimes of single Cik1-Kar3 under applied force**

One-micron size kinesin coated beads were prepared as described above. A bead was brought into contact with a segmented microtubule, whose polarity was identified by the presence of long and short extensions, and allowed to bind. Experiments were done either in the presence of 1 mM AMPPNP (Jena Bioscience) or 5 units/ml Apyrase (NEB). Load was applied to the bead by either engaging force-clamp along the microtubule axis or stepping along the microtubule for 150 – 300 nm. In many instances, stepping did not lead to any generation of the force as measured by the optical trap either because there was no motor on the bead or because the motor was not bound to the microtubule during the move. We performed control experiments in which beads were not incubated with kinesin beforehand. These beads showed no binding in 100% cases, which suggested that increase in tension was indeed due to force applied to the kinesin bound to the microtubule. After 2-3 weeks this number dropped to less than 90% and new beads were prepared.

One bead was probed several times for binding on 2 – 3 different microtubules during ~ 5 minute period after which a different bead was chosen for another test. In total we collected data applying force to either plus or minus end of microtubules to ~ 30 beads, which resulted in 250 – 300 measurements for each experimental condition (e.g. nucleotide state or type of molecule).

### **Live cell imaging of *Drosophila* S2 cells**

The cells were visualized using a confocal spinning disk (Visitron) using a 63x lens and 1.6 magnification or 150x lens and 1.2 magnification on Zeiss inverted microscope at RT. Cells were adhered to concanavalin A coated coverslips. Mitotic cells expressing low levels of EB1-GFP were imaged for ~ 2 minutes with 1 – 2 second intervals using 100 ms exposure per slice. Maximum intensity projections were made using Fiji and used for further analysis. Plus-end tips were tracked automatically using u-track (Jaqaman et al., 2008) or manually using MTrackJ.

Double stranded RNA (dsRNA) was produced for PCR-products using the megascript (thermofisher, AM1333). 350000 cells containing EB1-GFP were plated 2 hours before RNAi. dsRNA was mixed with 250µl SFM and 5µl cellfectin II (Invitrogen) 30 minutes before addition to the cells. Full media was removed gently to keep the cells in the 24-well and the dsRNA-mix was added. After 45 minutes 750µl of full media was added. After 3 days, 500µl of full media containing 300µM CuSO<sub>4</sub> was added to reach a final concentration of 100µM CuSO<sub>4</sub>. At day 4 cells were transferred to concanavalin coated dishes (5µg/µl) for 15 minutes prior to microscopy. dsRNA targeting the white gene was used as negative control.

### **ATPase assays**

ATPase assays have been performed using EnzChek Phosphate Assay Kit (Molecular Probes) according to the manufacturer protocol and using taxol stabilized microtubules. We found that freezing Cik1-Kar3 decreased its ATPase activity by ~ 30%, therefore we performed ATPase assays with freshly purified protein. In addition to the standard purification procedure Cik1-Kar3 was passed through a Superose 6 gel filtration column and then was used directly in the ATPase assay.

## QUANTIFICATION AND STATISTICAL ANALYSIS

### Image analysis

For the analysis and comparison between different experimental conditions, we picked data in which pellicles nucleated roughly the same amount of microtubules and those in which density of the nucleation centers was similar. Tracking of growing microtubule plus ends was done in the EB1 channel by the u-track software (Jaqaman et al., 2008). A custom-made algorithm designed in MATLAB was used to facilitate the classification the tracked ends, which for each individual tip was done by eye.

In order to obtain microtubule growth rate in the absence of EB1 microtubule ends were manually tracked using MTrackJ ImageJ plugin. Distributions and histograms were plotted using MATLAB.

### Analysis of high-resolution recordings of Cik1-Kar3 movement

In order to obtain histogram of step sizes of Cik1-Kar3 movement recordings of individual movements were fitted to a staircase-type function (Kerssemakers et al., 2006). The algorithm required an initial guess on the approximate location of steps, and then varied the position and size of the step in order to identify the best fit, which yielded the size distribution of steps.

For fitting detachment lifetime data to the equation (1) a custom-made algorithm was written in MATLAB. Posterior distributions of parameters  $k_0$ ,  $D$  and  $d$  have been obtained by MCMC sampling and have been used to extract MAP values and 95% confidence intervals (Table S1). The software is available upon request.

## **Simulation of microtubule dynamics grown from tetrahymena pellicles in the presence of EB1 and Cik1-Kar3**

All simulations were done in 2D. Position of nucleation centers, angles at which microtubules nucleate as well as parameters of dynamics instability were taken from experimental data obtained in the absence of Cik1-Kar3 (Figure S3A,B). Microtubule growth rate was set to 3.5  $\mu\text{m}/\text{min}$ , shrinking rate 40  $\mu\text{m}/\text{min}$ , catastrophe rate 0.007  $\text{sec}^{-1}$ . Based on our experimental data we assumed zero rescue rate, therefore shrinking microtubules fully disassembled and then resumed growth as soon as they reached zero length. All microtubules in the simulation were separated into either growing or shrinking and growing independently or guided. In the first case, direction of their growth was determined by the original orientations, which were extracted from the experimental data. For the guided microtubules, direction was defined by the orientation of the leading microtubule that guided the growth. Each iteration of Monte-Carlo simulation consisted of three steps. 1) Lengths of all microtubules were updated based on their states (growing or shrinking). For all growing microtubules, probability of catastrophe was calculated and the state was changed accordingly. 2) In the presence of Cik1-Kar3, orientations of guided microtubules were updated to make sure their trajectories coincide with guiding microtubules. 3) In the presence of Cik1-Kar3, ends of all freely growing microtubules that approached other microtubules within 100 nm were assumed to be captured and state of the microtubule was changed from independently growing to guided.

Additionally we assumed that when template microtubule undergoes catastrophe and shrinks, orientation of the guided microtubule that becomes free goes back to its original value. This was

also true for the guided microtubule that terminated its interaction and returned to the original angle as soon as it underwent a catastrophe.

The simulation was initiated with all microtubule lengths set to zero and let evolve until the fraction of guided microtubules reached steady state (Figure S3E). The steady state value was taken to plot the data (Figures S3C,D).

### **Simulation of the bundle formation at the shmoo tip**

The simulation was done exactly as described above. Walls of the yeast cell were described by pear-shaped function:

$$r^2 = (x^2 + y^2)(1 + 2x + 5x^2 + 6x^3 + 6x^4 + 4x^5 + x^6 - 3y^2 - 3xy^2 - 2x^2y^2 + 8x^2y^2 + 8x^3y^2 + 3x^4y^2 + 2y^4 + 4xy^4 + 3x^2y^4 + y^6)$$

Coordinates were scaled and shifted such that the cell has characteristic size  $\sim 5$  microns. We assumed that microtubules undergo catastrophe as soon as they touch surface of the cell or the nucleus (Movie S6), which was modeled as a circle with 2.4-micron diameter. For the simulation of the stabilization effect, we assumed that all microtubules that reach shmoo tip within 0.5 rad angle get attached to the tip and have a low probability of undergoing catastrophe ( $0.002 \text{ sec}^{-1}$ ) (Movie S5). Microtubule growth rate in these simulations was  $1 \mu\text{m}/\text{min}$ , microtubule catastrophe rate  $5 \mu\text{m}/\text{min}$ . In order to extract the probability that microtubule bundle points to the shmoo tip (Figure 7F), the simulation was allowed to run to obtain one hour of dynamics and then the probability was calculated as ratio between the cumulative times when there was at least one microtubule connected to the shmoo tip to the overall time of the simulation.

## Mathematical model of Cik1-Kar3 movement

Average velocity of Cik1-Kar3 movement equals average step size of Cik1-Kar3 per single ATP hydrolysis divided by the time it takes to finish one nucleotide addition cycle:

$$v = \frac{d}{t_0} \quad (2)$$

The time  $t_0$  depends on the kinetic constants of the ATP cycle and does not depend on the particular potential landscape of interaction between Cik1-Kar3 and tubulin. Given that forces that can stall movement of Cik1-Kar3 are small (Figure 4C) we will assume that this time also does not depend on the external force, and treat it an independent parameter.

The average step per one ATP cycle consists of two components:

$$d = h_0 p + d_2 \quad (3)$$

Here  $h_0$  is size of the tubulin dimer,  $p$  - probability that binding of ATP results in productive step towards the minus end;  $d_2$  – average displacement during random movement in weakly bound ADP state.

Bound Cik1-Kar3 experiences thermal forces from surrounding media that induce its motion, restricted by the width of the potential well. The change in the potential energy associated with the movement follows the Boltzmann statistics:

$$p(x) \sim e^{-\frac{E(x)}{k_B T}} \quad (4)$$

Where  $p$  is the probability of Cik1-Kar3 being at the spatial coordinate  $x$  and  $E(x)$  is the potential energy landscape. Probability of making a step caused by changes of the potential landscape from no NTP to ATP depends on the probability of the Cik1-Kar3 to shift due to thermal fluctuations to the position towards the minus end along the microtubule axis for more than  $\Delta_1 = (D-\delta)_{ATP}$  – distance from the minimum of the potential energy to the highest energy in the ATP state (Figure 5D). In this case, when potential landscape changes to ATP state it will be trapped by the potential of the next tubulin subunit. This probability is given by:

$$p = A \int_1^2 e^{-\frac{E_{noNTP}(x) - Fx}{k_B T}} dx, \quad (5)$$

Where  $A$  – normalization constant;  $E_{noNTP}$  potential energy landscape in no NTP state;  $F$  – external opposing force;  $x$  – special coordinate towards the microtubule minus end;  $\Delta_2 = (D+\delta)_{noNTP}$  – distance from the minimum of the potential energy to the highest energy in the no NTP state.

Because forces are small  $F \cdot x < k_B T$ , therefore:

$$p = A \int_1^2 e^{-\frac{E(x)}{k_B T}} \left(1 + \frac{F \cdot x}{k_B T}\right) dx = A \int_1^2 e^{-\frac{E(x)}{k_B T}} dx + \frac{F}{k_B T} A \int_1^2 e^{-\frac{E(x)}{k_B T}} x dx \quad (6)$$

This can be rewritten as following:

$$p = \left( \int_1^2 e^{-\frac{E(x)}{k_B T}} dx + \frac{F}{k_B T} \int_1^2 e^{-\frac{E(x)}{k_B T}} x dx \right), \quad (7)$$

where integrals  $\hat{E}_1$  and  $\hat{E}_2$  depend only on the particular shape of the function  $E_{noNTP}(x)$

Second term in (2) can be written as:

$$d_2 = \bar{v} \cdot t_{ADP} \quad (8)$$

Where  $\bar{v}$  is the average velocity of diffusion in ADP state under applied force,  $t_{ADP}$  – average time that the molecule spends in diffusive ADP state.

Assuming force of the optical trap is balanced by the drag force. Therefore:

$$d_2 = \frac{F}{\zeta} t_{ADP} = \frac{F D_{ADP}}{k_B T} t_{ADP} \quad (9)$$

Here  $\zeta_{ADP}$  is frictional coefficient and  $D_{ADP}$  is the diffusion coefficient in the ADP state (Mieck et al., 2015).

Combining (6) and (8) together average velocity of Cik1-Kar3 movement is

$$v = \frac{1}{t_o} (h_o (D + \Delta D) - E_1 - \frac{F}{k_B T} E_2) F \frac{D_{ADP}}{k_B T} t_{ADP} \quad (10)$$

, where  $\Delta D$  is the difference between widths of the potentials in the no NTP and ATP states,  $\Delta\delta$  is the difference between asymmetries of these potentials (Figure 5D). Equation (10) directly shows that velocity of Cik1-Kar3 movement depends linearly on the differences between  $D$  and  $\delta$  parameters of the potentials in the no NTP and ATP states (Figure 5D). This provides a direct demonstration how change in the asymmetry of the potential can drive the movement of the motor.

## DATA AND SOFTWARE AVAILABILITY

Data and software are available from the corresponding author upon request.

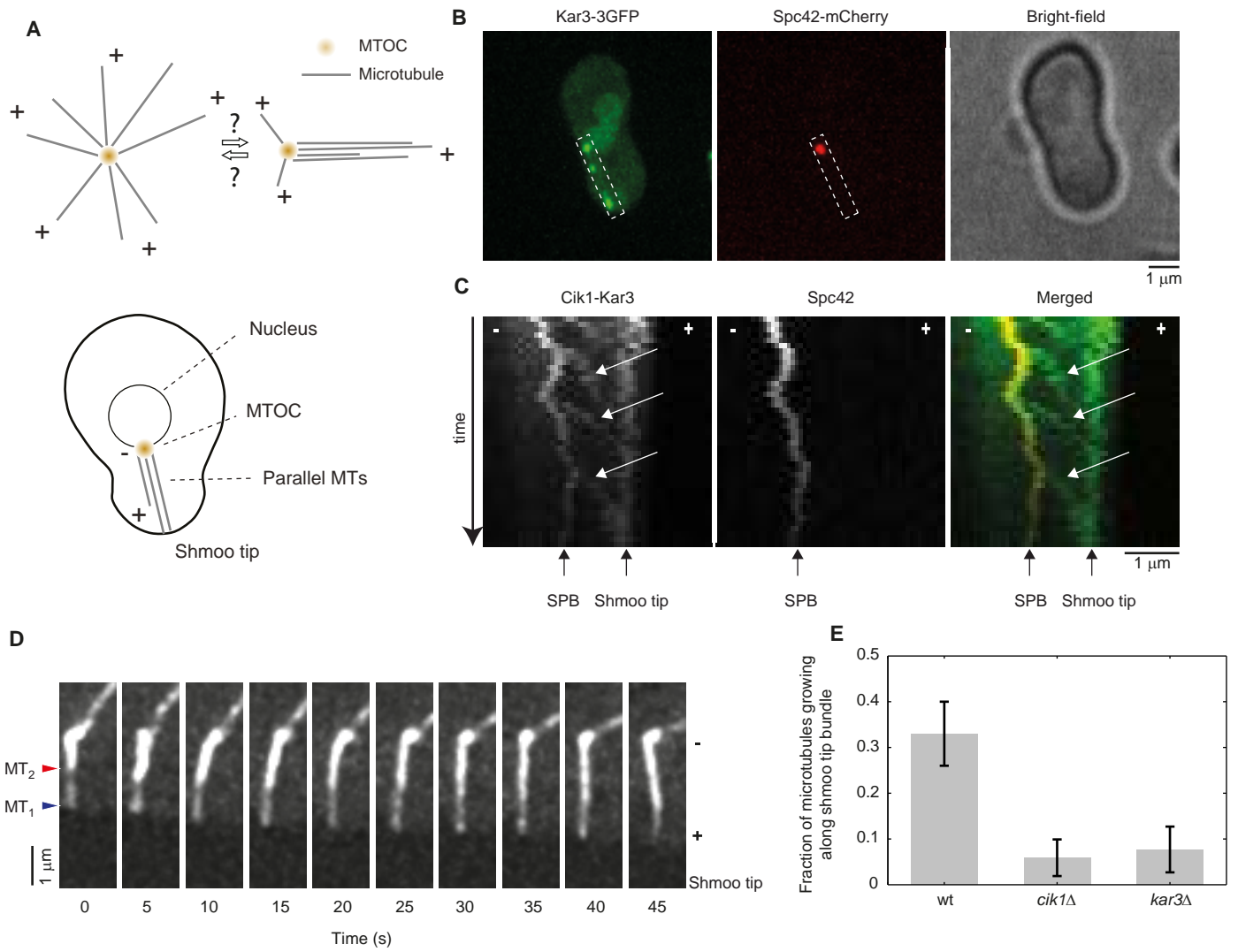


Figure 1

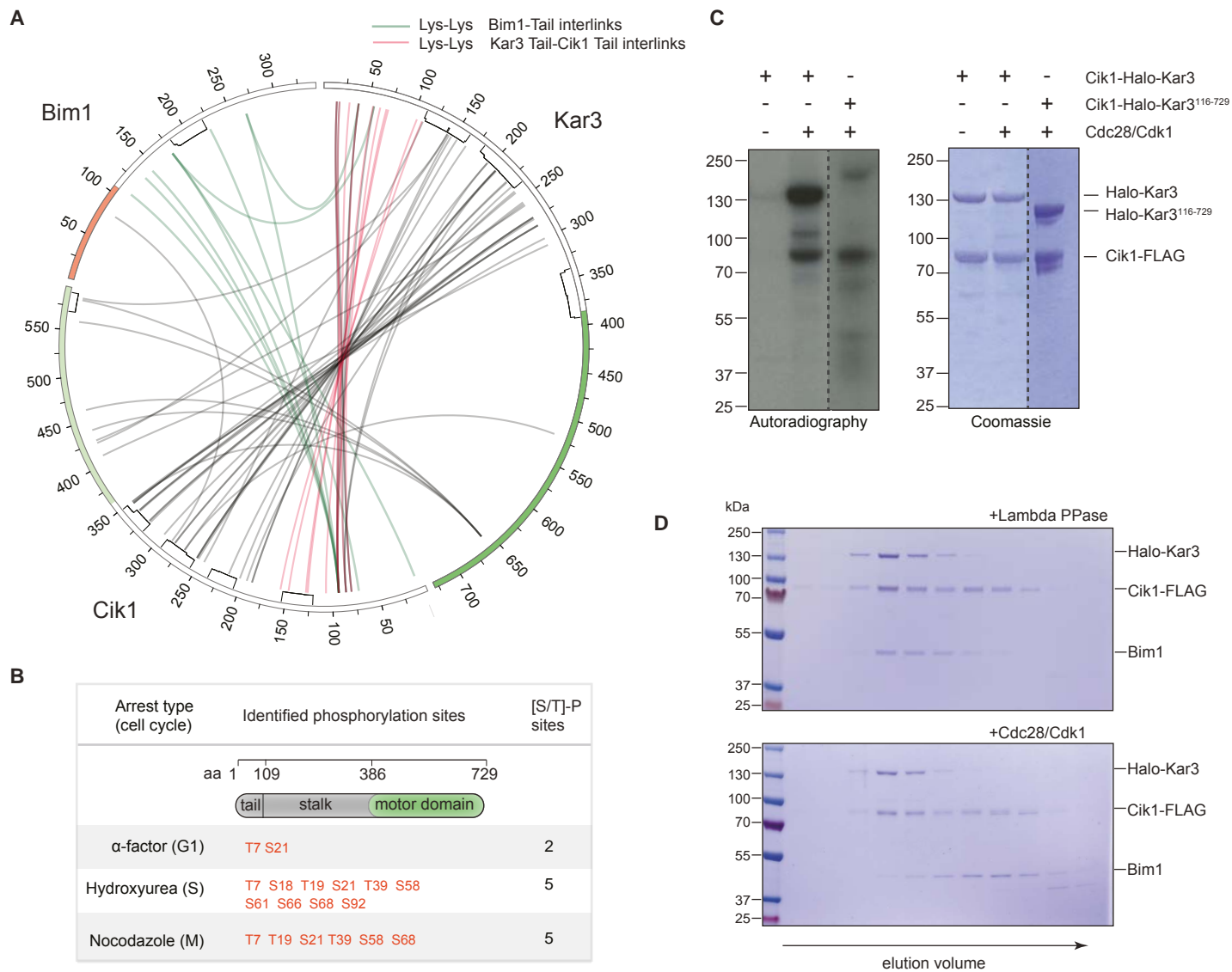


Figure 2

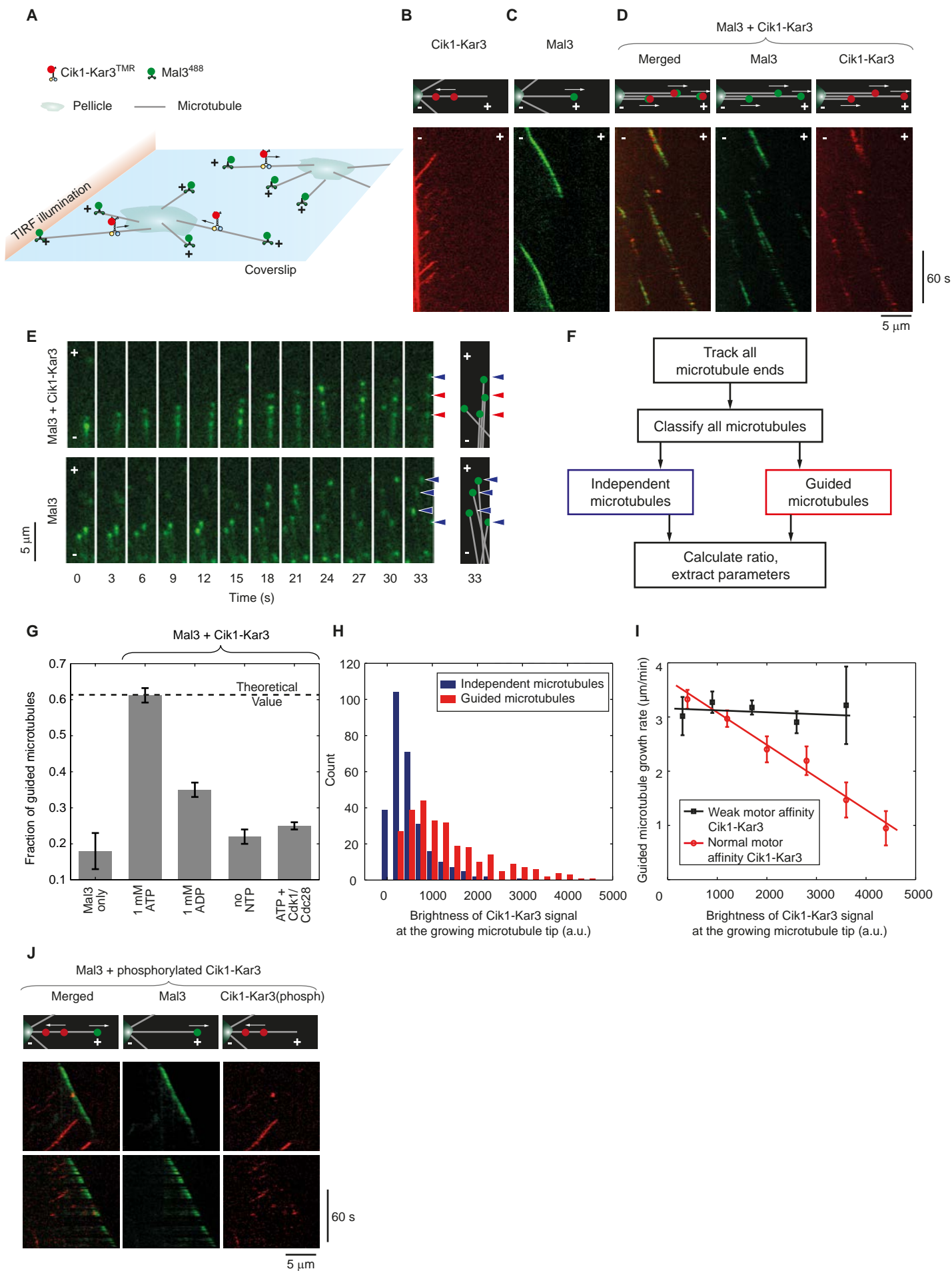


Figure 3

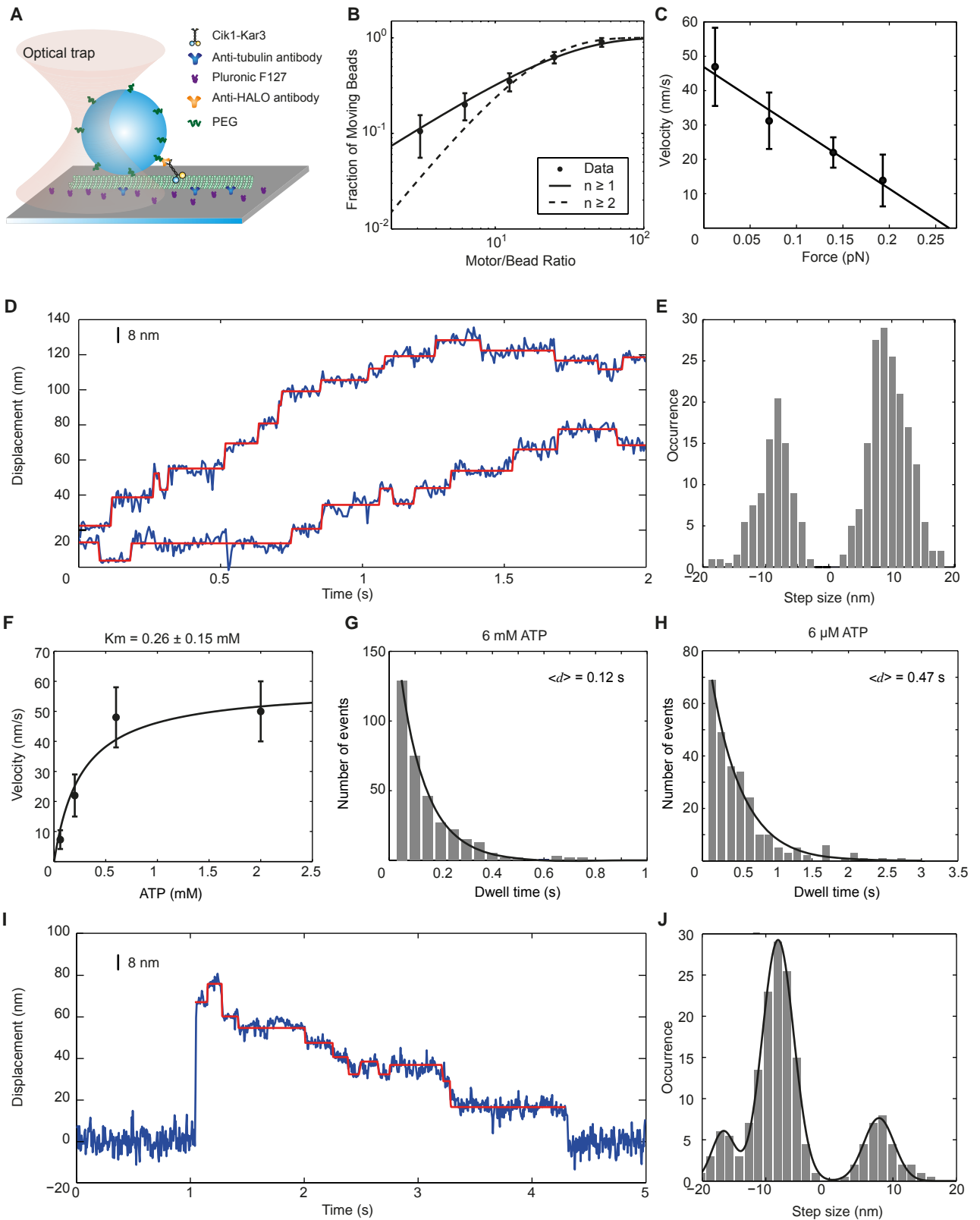
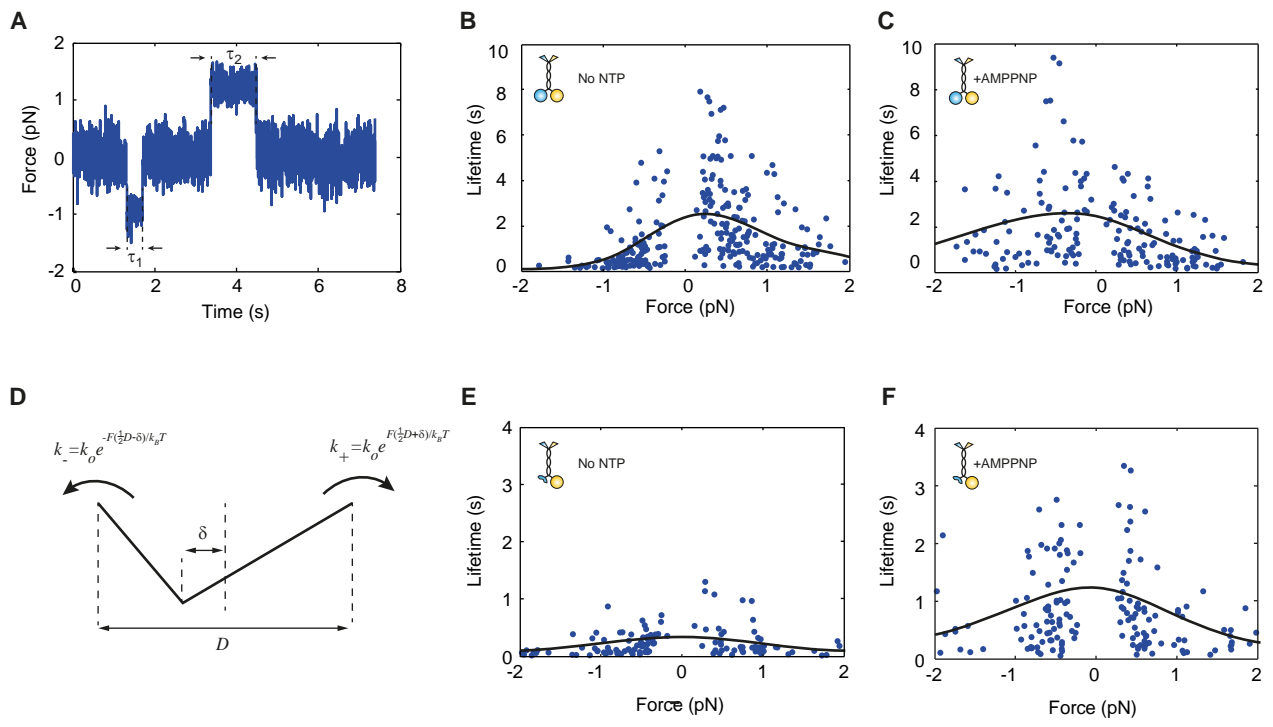


Figure 5



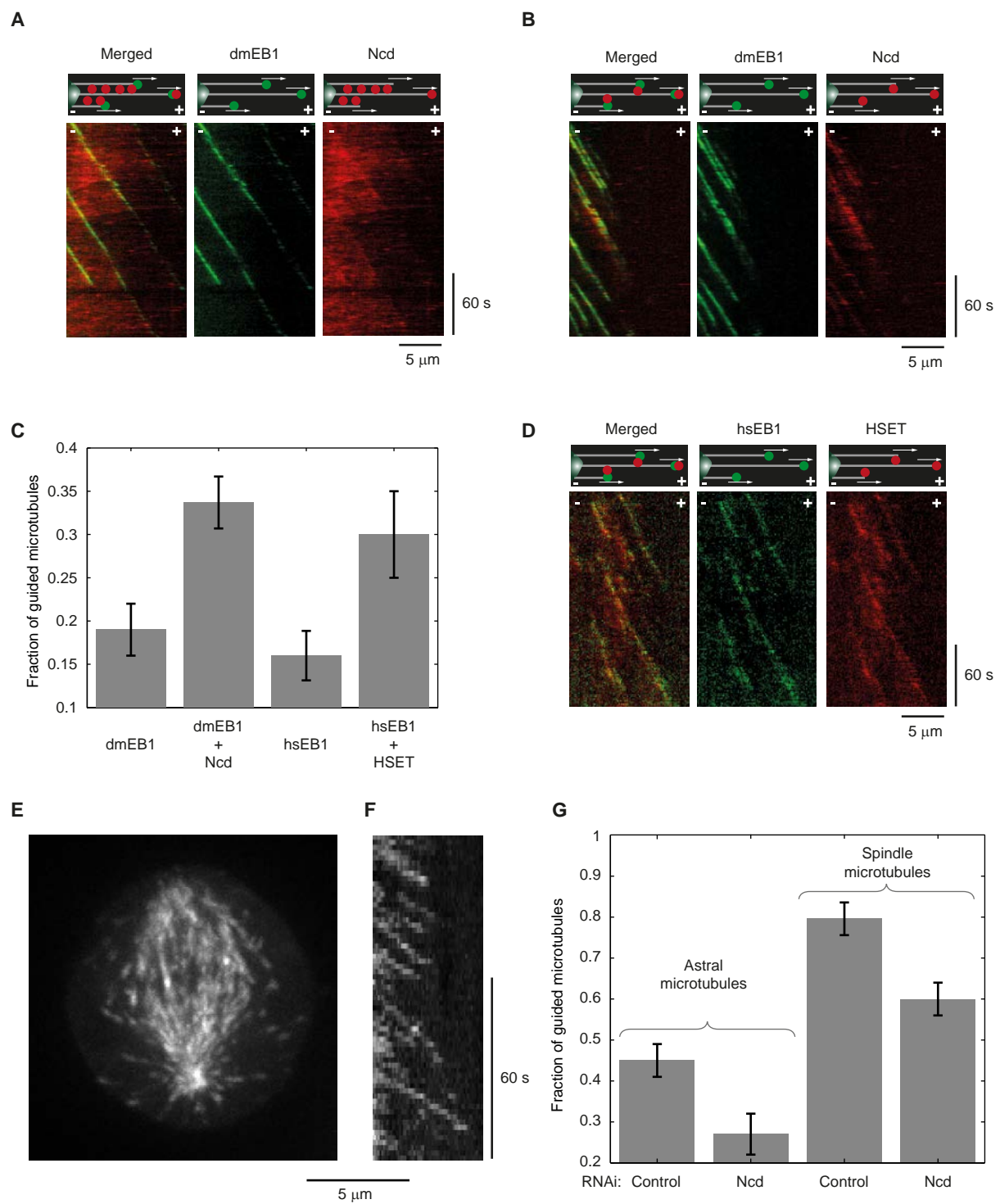


Figure 6

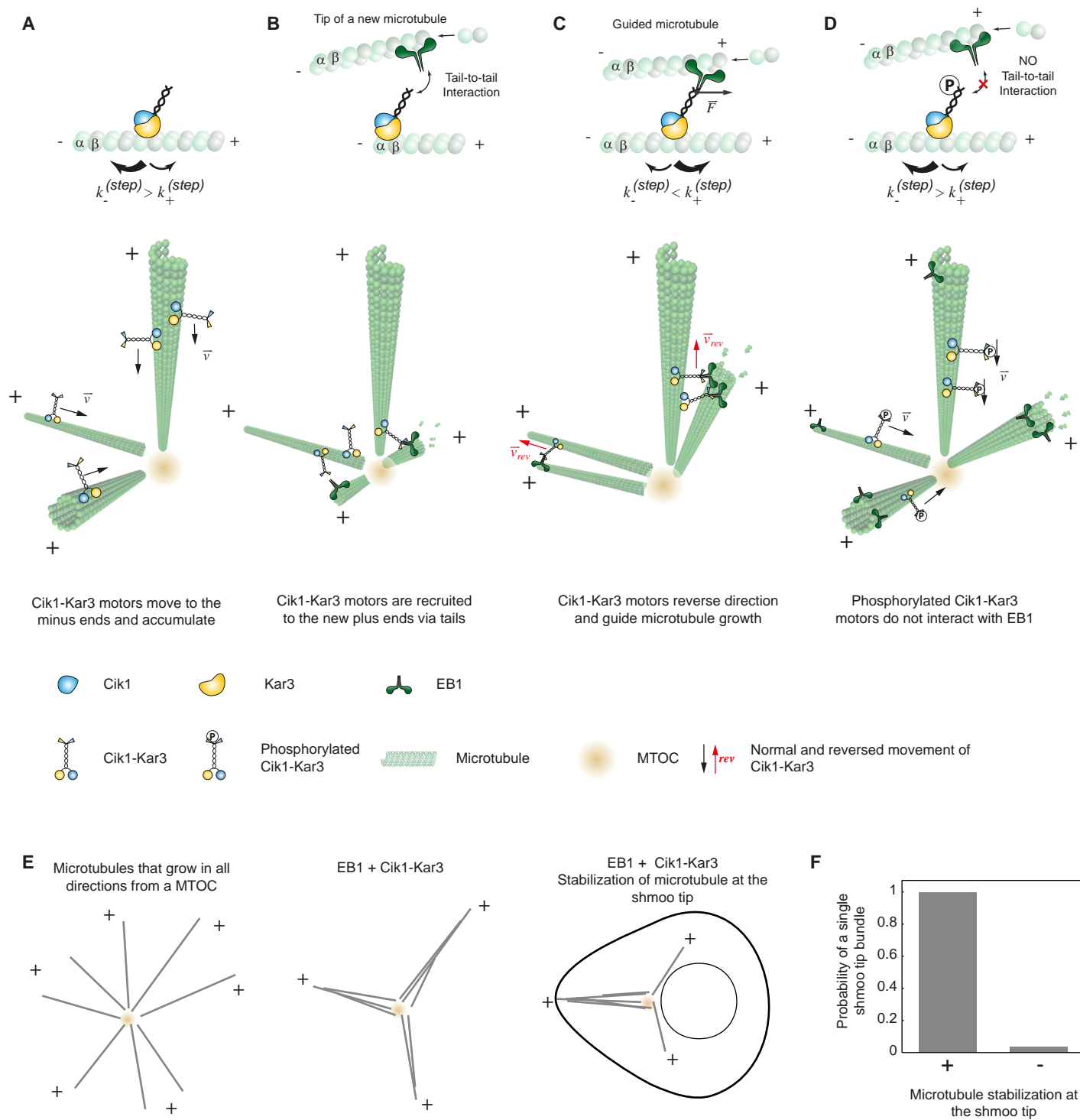


Figure 7

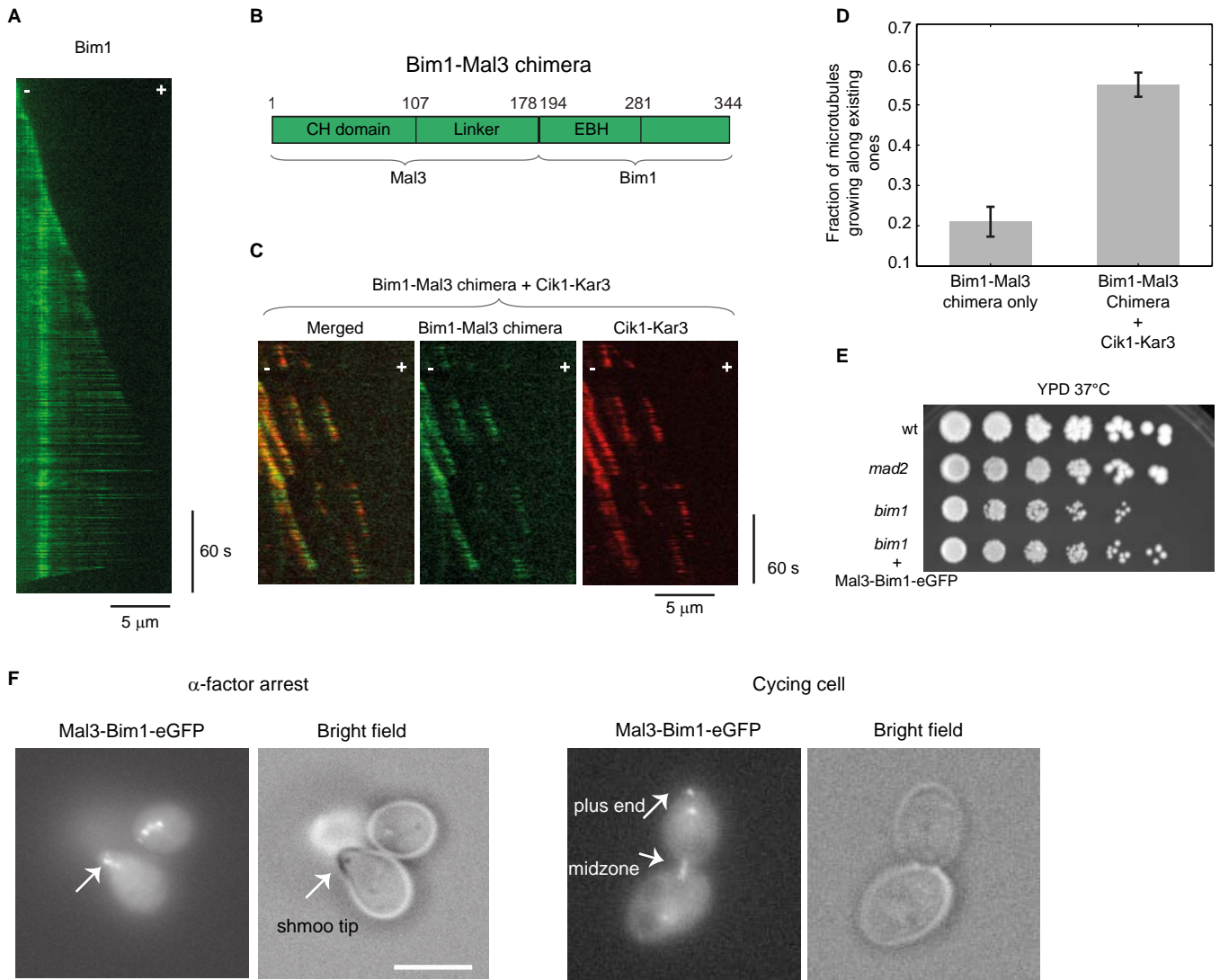


Figure S1

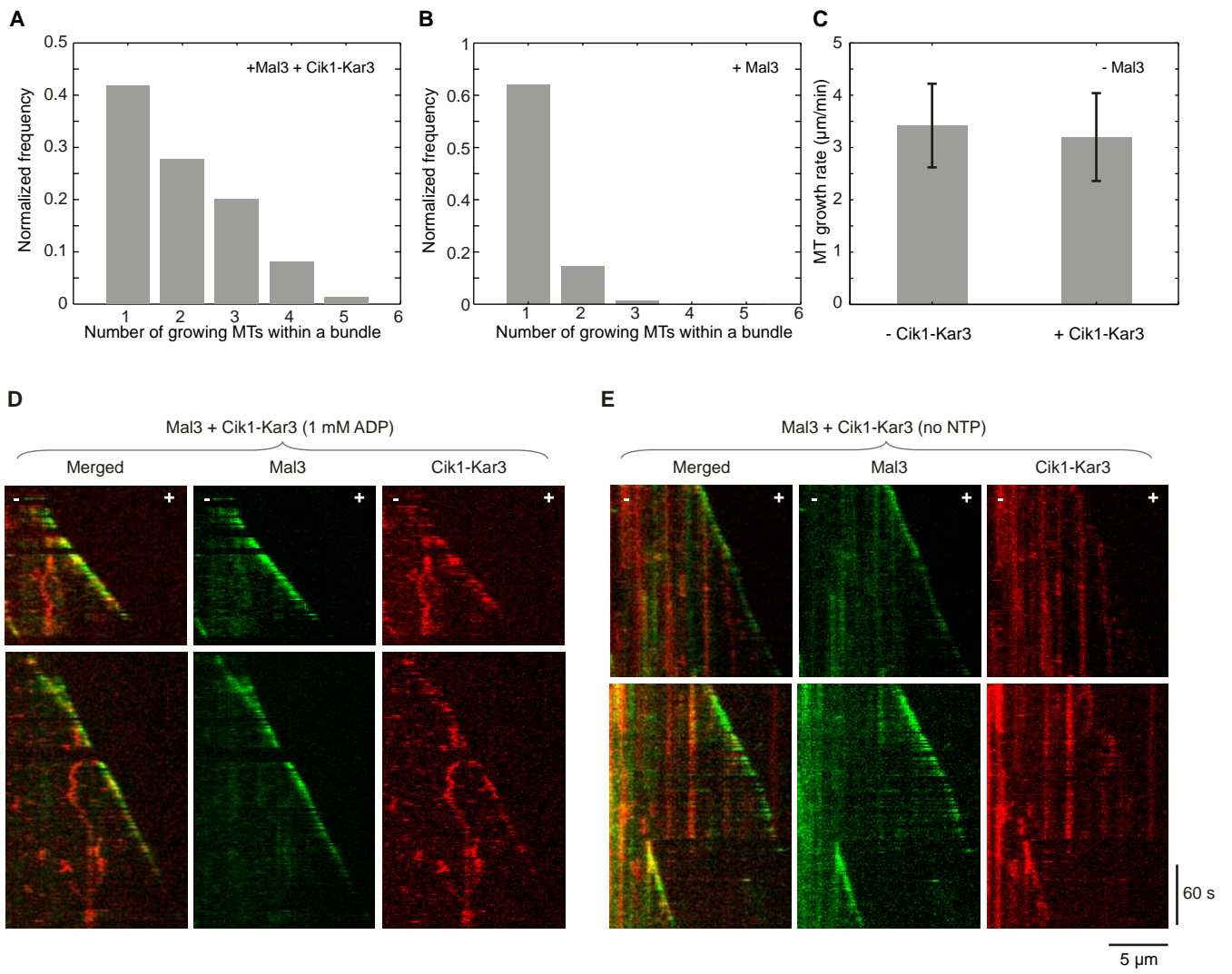


Figure S2

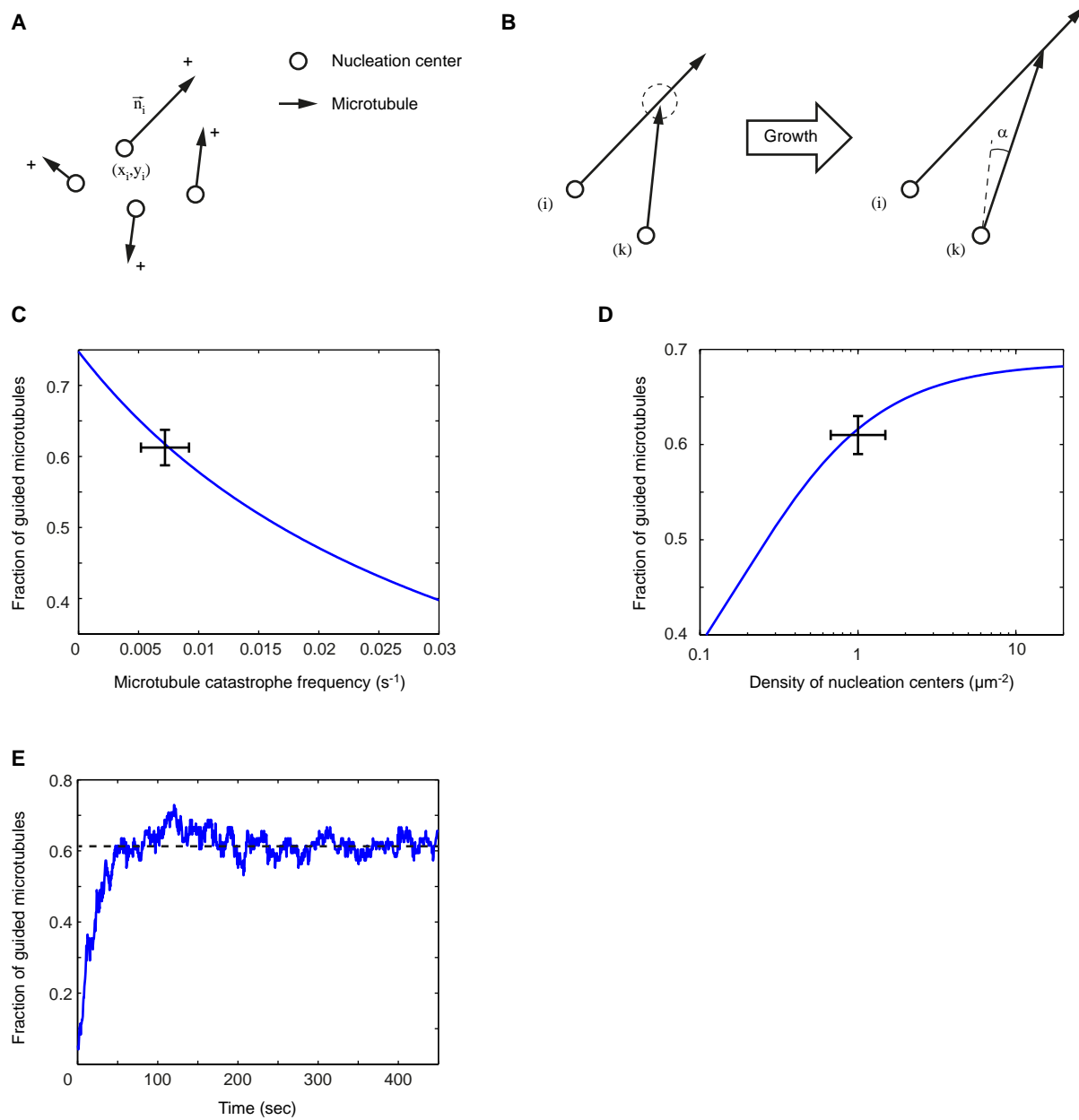


Figure S3

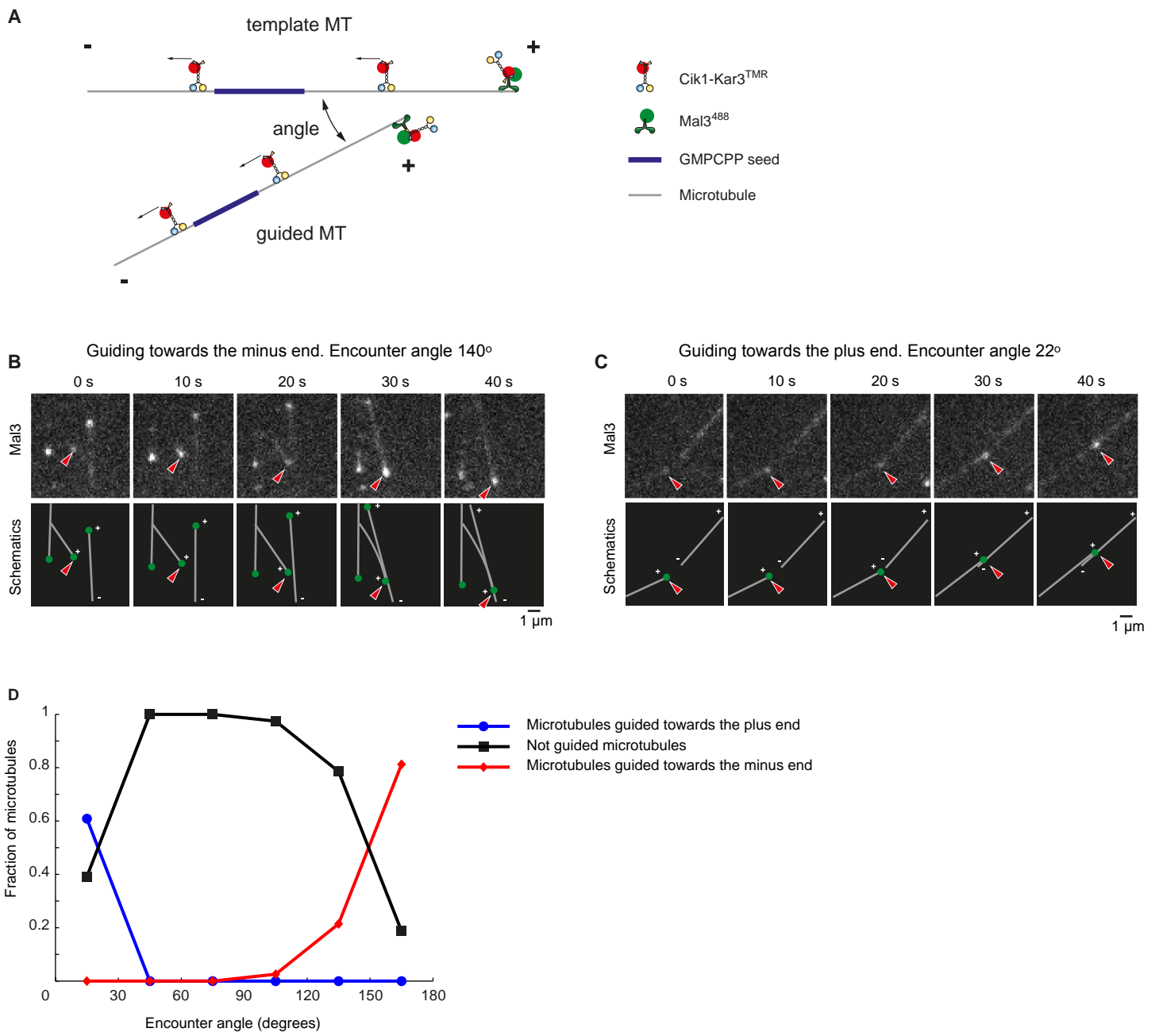


Figure S4

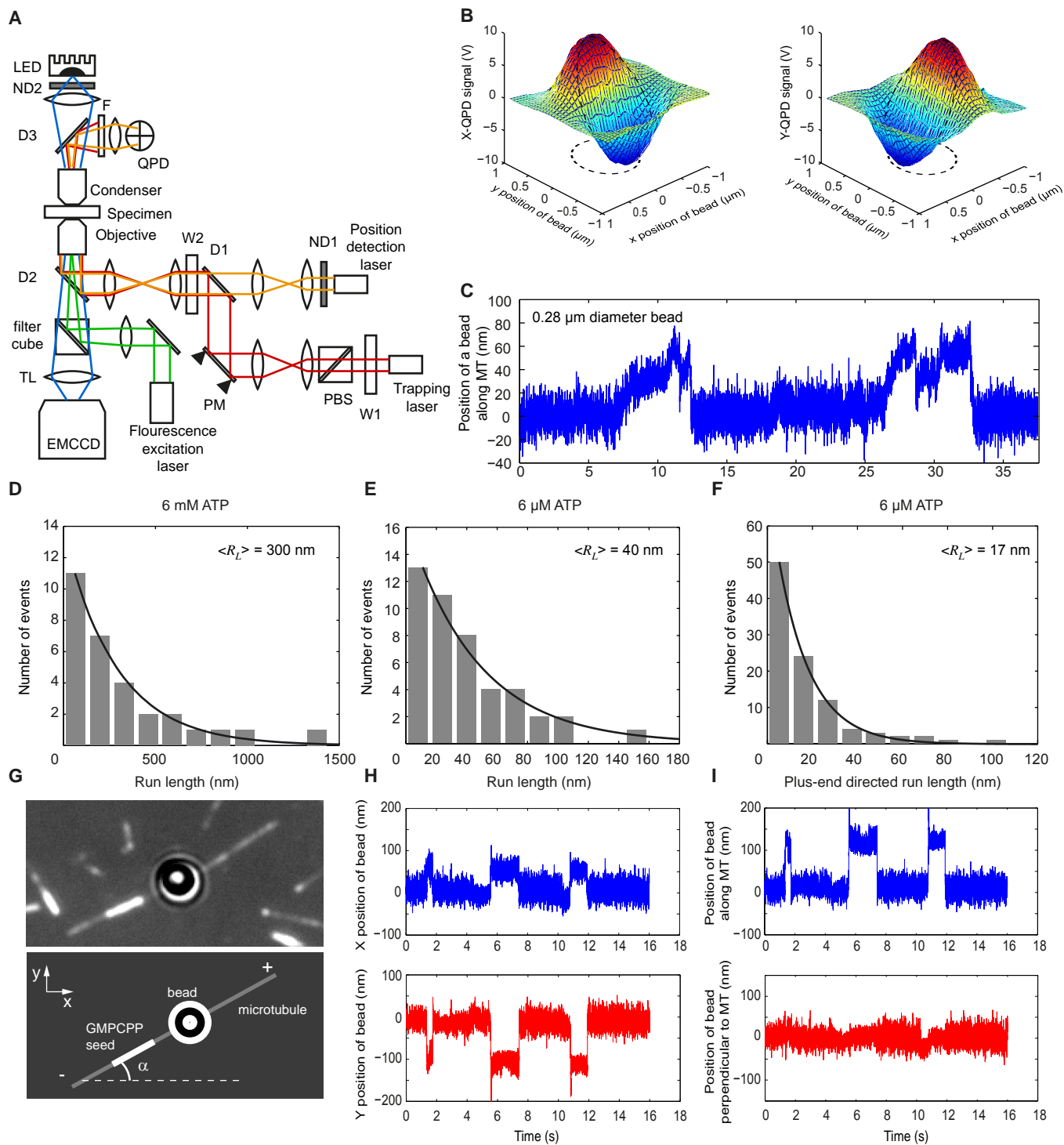


Figure S5

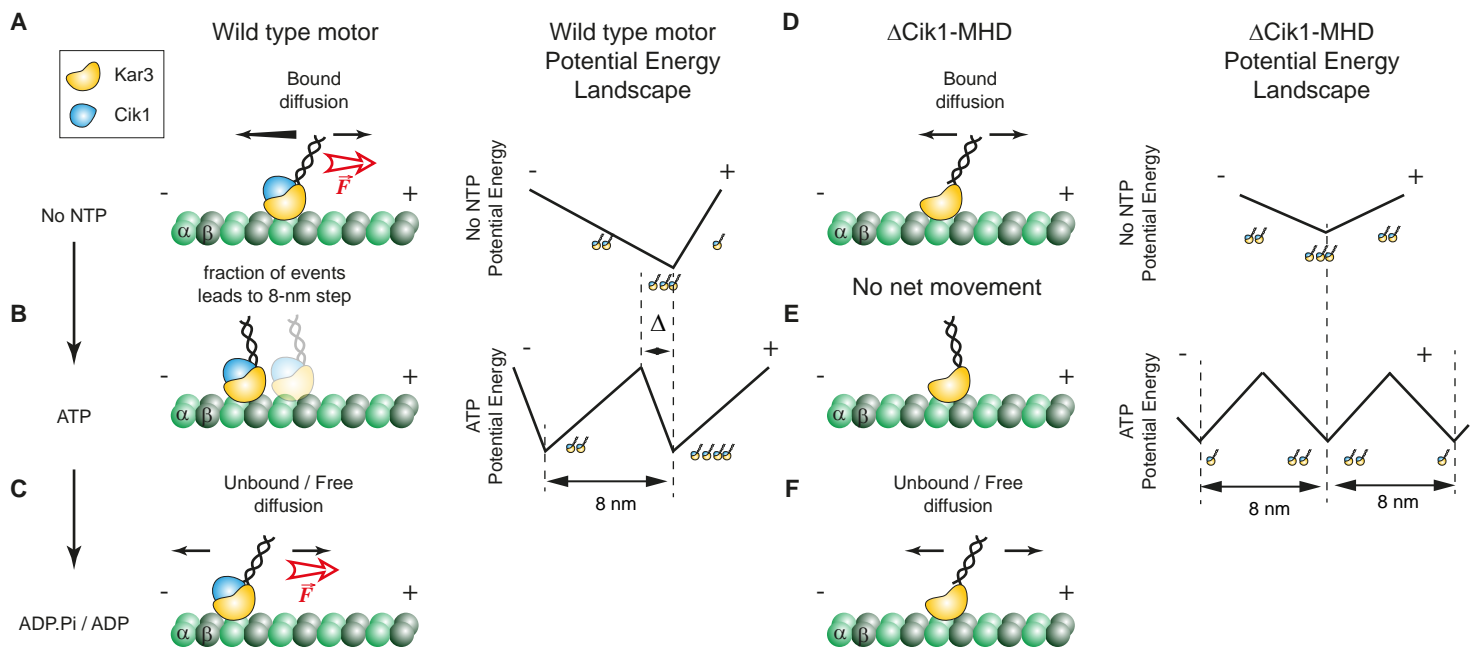


Figure S6

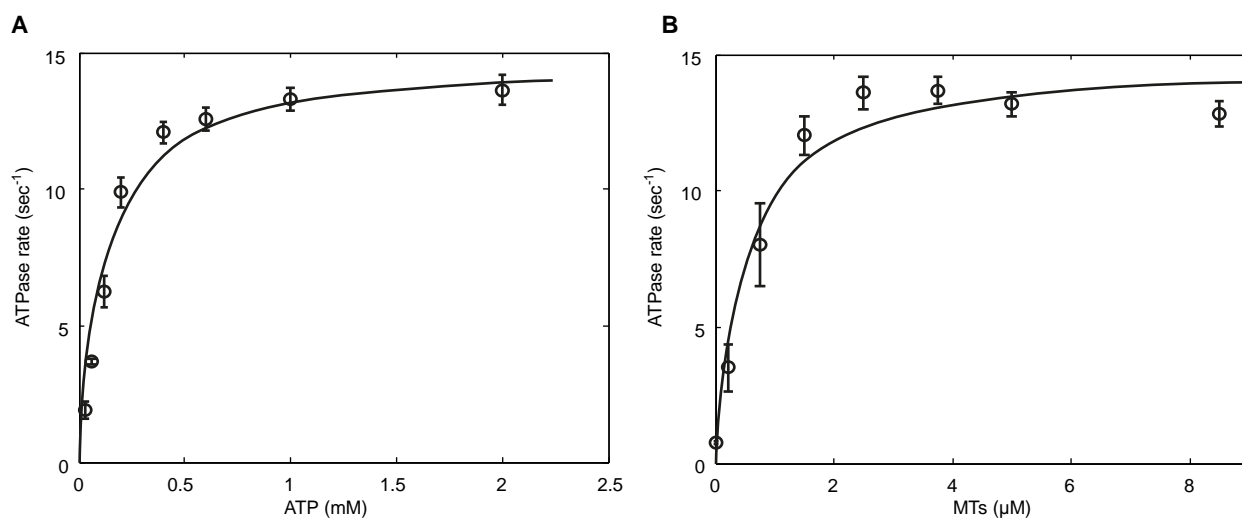


Figure S7

**Table S1. Parameters of the interaction potentials between Cik1-Kar3 and microtubule lattice for wt and mutant molecules in no NTP and AMPPNP states (Figure 5D). Errors are 95% confidence intervals.**

Molecule	ATP state	$k_o$ ( $s^{-1}$ )	$D$ (nm)	$\delta$ (nm)
wt	No NTP	$0.21 \pm 0.02$	$12.1 \pm 0.9$	$-2.3 \pm 0.4$
	AMPPNP	$0.20 \pm 0.02$	$8.5 \pm 0.9$	$1.4 \pm 0.6$
Cik1 <sup>(1-360)</sup> -Kar3	No NTP	$1.3 \pm 0.2$	$10.2 \pm 1$	$0.0 \pm 0.5$
	AMPPNP	$0.42 \pm 0.04$	$7.8 \pm 0.7$	$0.4 \pm 0.4$

# DuEPublico

Duisburg-Essen Publications online

UNIVERSITÄT  
DUISBURG  
ESSEN

*Offen im Denken*

ub

universitäts  
bibliothek

This text is made available via DuEPublico, the institutional repository of the University of Duisburg-Essen. This version may eventually differ from another version distributed by a commercial publisher.

**DOI:** 10.1016/j.cell.2016.09.029

**URN:** urn:nbn:de:hbz:464-20200310-143406-3



This work may be used under a Creative Commons Attribution - NonCommercial - NoDerivatives 4.0 License (CC BY-NC-ND 4.0)